LETTER

A human neurodevelopmental model for Williams syndrome

Thanathom Chailangkarn[1,2,3,4]*, Cleber A. Trujillo[1,2,3]*, Beatriz C. Freitas[1,2,3], Branka Hrvoj-Mihic[5], Roberto H. Herai[1,2,3,6], Diana X. Yu[7], Timothy T. Brown[8,9,10], Maria C. Marchetto[7], Cedric Bardy[7,11], Lauren McHenry[7], Lisa Stefanacci[1,2,3,5]‡, Anna Järvinen[12], Yvonne M. Searcy[12], Michelle DeWitt[12], Wenny Wong[12], Philip Lai[12], M. Colin Ard[9], Kari L. Hanson[5], Sarah Romero[1,2,3], Bob Jacobs[13], Anders M. Dale[8,14,15], Li Dai[16,17], Julie R. Korenberg[16,17], Fred H. Gage[7,18], Ursula Bellugi[12], Eric Halgren[8,9,18], Katerina Semendeferi[5,18,19] & Alysson R. Muotri[1,2,3,18,19]

Williams syndrome is a genetic neurodevelopmental disorder characterized by an uncommon hypersociability and a mosaic of retained and compromised linguistic and cognitive abilities. Nearly all clinically diagnosed individuals with Williams syndrome lack precisely the same set of genes, with breakpoints in chromosome band 7q11.23 (refs 1–5). The contribution of specific genes to the neuroanatomical and functional alterations, leading to behavioural pathologies in humans, remains largely unexplored. Here we investigate neural progenitor cells and cortical neurons derived from Williams syndrome and typically developing induced pluripotent stem cells. Neural progenitor cells in Williams syndrome have an increased doubling time and apoptosis compared with typically developing neural progenitor cells. Using an individual with atypical Williams syndrome[6,7], we narrowed this cellular phenotype to a single gene candidate, frizzled 9 (*FZD9*). At the neuronal stage, layer V/VI cortical neurons derived from Williams syndrome were characterized by longer total dendrites, increased numbers of spines and synapses, aberrant calcium oscillation and altered network connectivity. Morphometric alterations observed in neurons from Williams syndrome were validated after Golgi staining of post-mortem layer V/VI cortical neurons. This model of human induced pluripotent stem cells[8] fills the current knowledge gap in the cellular biology of Williams syndrome and could lead to further insights into the molecular mechanism underlying the disorder and the human social brain.

This study included participants with a clinical diagnosis of Williams syndrome (WS): individuals harbouring typical gene deletions in the Williams–Beuren syndrome critical region[1,9] (WS17, 25, 77 and 79) and an individual with atypical WS with a partial deletion (pWS88) as well as typically developing (TD) participants (TD55, 59, 63 and 70) (Fig. 1a and Extended Data Fig. 1a). After a series of cognitive and social profiles[2,5,10], we confirmed that the individuals with typically deleted WS were a representative cohort of the disorder (Fig. 1b–c, Extended Data Fig. 1b–g and Supplementary Note 1). To generate a human cellular model of WS[11,12], dental pulp cells (DPCs) obtained from participants' deciduous teeth were reprogrammed into induced pluripotent stem cells (iPSCs) (Extended Data Fig. 2a). We selected two to three clones from each individual for further investigation (Extended Data Fig. 2b–g and Supplementary Tables 1 and 2). To obtain the relevant cells, iPSC clones underwent neural induction (Fig. 1d) and neural progenitor cells (NPCs) were further characterized (Fig. 1e–g). Cortical neurons were obtained using a modified protocol from our previous publication[11] (Fig. 1h–j). Finally, iPSC-derived neurons exhibited a complete set of electrophysiological properties (Fig. 1k–m and Extended Data Fig. 2h, i).

The impact of the genome-wide Williams–Beuren syndrome chromosome region deletion was determined by unbiased RNA sequencing (RNA-seq) (Extended Data Fig. 3a–d). Differential expression analyses revealed misregulated genes among the three genotypes (Extended Data Fig. 3e–h, Extended Data Table 1 and Supplementary Tables 3–9). Gene ontology (GO) analyses of NPCs and neurons revealed biological processes relevant to the condition (Extended Data Fig. 3h, i, Extended Data Table 2 and 3 and Supplementary Table 10). Remarkably, 'cell adhesion', 'axon guidance' and 'cell maturation' were also among the top-ranking categories detected in an independent publication using WS NPC gene expression analysis[13].

As suggested by the NPC global gene expression analyses, during the culture maintenance, typical WS NPCs became confluent more slowly than TD NPCs (Fig. 2a). After plating the same number of NPCs, we verified that the number of typical WS NPCs on day 4 was less than the TD NPCs (Fig. 2b and Extended Data Fig. 4a). To rule out the possibility that the difference in heterogeneity of iPSC-derived NPCs could result in this observation, the NPC population was fully characterized and no difference between WS and TDs were found (Fig. 1e–g and Extended Data Fig. 4b). We also used single-cell gene expression profiling to access the homogeneity of the NPCs (Fig. 2c–e and Extended Data Fig. 4c–g). We further investigated the proliferation of WS NPCs by performing BrdU labelling, immunostaining and fluorescence-activated cell sorting (FACS) (Extended Data Fig. 4h, i). Since no difference was found, we assessed apoptosis in WS NPCs using DNA fragmentation (propidium iodide) and caspase assay (Extended Data Fig. 4j). We found a significant increase in subG1

[1]University of California San Diego, School of Medicine, UCSD Stem Cell Program, Department of Pediatrics/Rady Children's Hospital San Diego, La Jolla, California 92037, USA. [2]University of California San Diego, School of Medicine, Department of Cellular & Molecular Medicine, La Jolla, California 92037, USA. [3]Center for Academic Research and Training in Anthropogeny (CARTA), La Jolla, California 92093, USA. [4]National Center for Genetic Engineering and Biotechnology (BIOTEC), Virology and Cell Technology Laboratory, Pathum Thani 12120, Thailand. [5]University of California San Diego, Department of Anthropology, La Jolla, California 92093, USA. [6]Graduate Program in Health Sciences, School of Medicine, Pontifícia Universidade Católica do Paraná (PUCPR), Curitiba, Paraná, Brazil. [7]The Salk Institute for Biological Studies, Laboratory of Genetics, La Jolla, California 92037, USA. [8]University of California San Diego, Multimodal Imaging Laboratory, La Jolla, California 92093, USA. [9]University of California San Diego, School of Medicine, Department of Neurosciences, La Jolla, California 92093, USA. [10]University of California San Diego, Center for Human Development, La Jolla, California 92093, USA. [11]SAHMRI Mind & Brain Theme, Laboratory for Human Neurophysiology and Genetics, Flinders University School of Medicine, Adelaide, South Australia 5000, Australia. [12]The Salk Institute for Biological Studies, Laboratory for Cognitive Neuroscience, La Jolla, California 92037, USA. [13]Colorado College, Department of Psychology, Colorado Springs, Colorado 80903, USA. [14]University of California San Diego, School of Medicine, Department of Radiology, La Jolla, California 92093, USA. [15]University of California San Diego, Department of Cognitive Science, La Jolla, California 92093, USA. [16]University of Utah, Department of Pediatrics, Salt Lake City, Utah 84108, USA. [17]University of Utah, The Brain Institute, Salt Lake City, Utah 84108, USA. [18]University of California San Diego, Kavli Institute for Brain and Mind, La Jolla, California 92093, USA. [19]University of California San Diego, School of Medicine, Neuroscience Graduate Program, La Jolla, California 92093, USA.
*These authors contributed equally to this work.
‡Deceased.
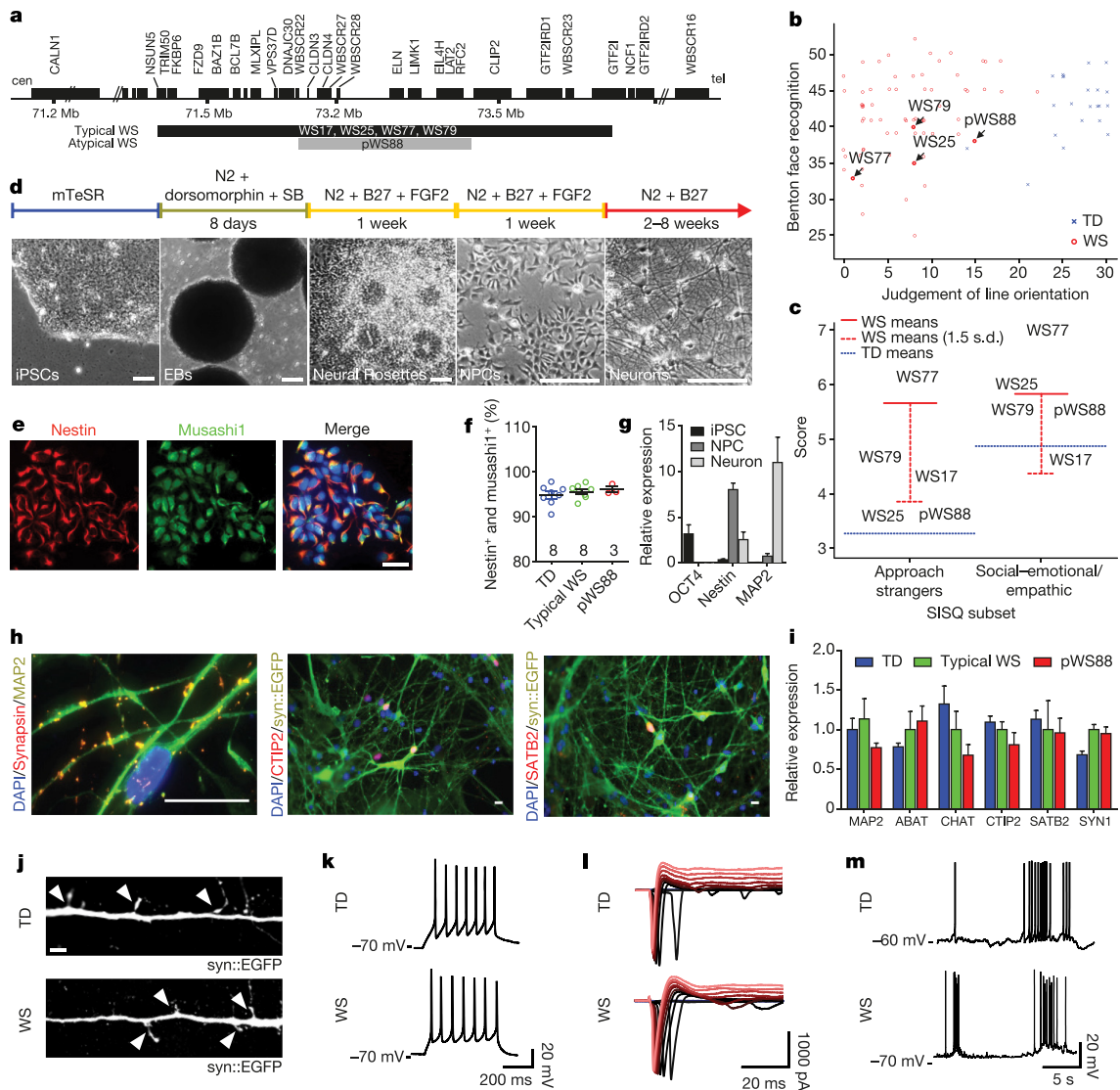
Figure 1 | Characterization of participating individuals and iPSC differentiation. a, Diagram showing genes and deletion region of individuals with WS. **b**, Scatter plot of Benton Face Recognition and Judgment of Line Orientation scores (jitter added) for $n = 69$ individuals with WS and $n = 22$ TD participants. **c**, Mean test scores for WS (solid red lines; $n = 101$ for approach strangers; $n = 100$ for social–emotional/empathic) and for TD individuals (dotted blue lines; $n = 80$ for approach strangers; $n = 79$ for social–emotional/empathic). **d**, Neural induction and neuronal differentiation protocol. Scale bar, $50\,\mu m$. **e**, Stage-specific protein expression in iPSC-derived NPCs. Scale bar, $50\,\mu m$. **f**, High percentage of Nestin and Musashi1-positive population was comparably

observed in TD, typical WS and pWS88 NPCs by FACS. Data are shown as mean $\pm$ s.e.m.; n, number of clones. **g**, Stage-specific markers for iPSC (*OCT4*), NPC (Nestin) and neuron (*MAP2*) by quantitative PCR (qPCR). **h**, Stage-specific protein expression in 6-week-old neurons. Scale bar, $25\,\mu m$. **i**, Expression of different neuronal markers in neurons indicating multiple neuronal subtypes in 6-week-old culture by qPCR. Data are shown as mean $\pm$ s.e.m. **j**, A representative image of neuronal protrusions (spine-like, arrowheads) from iPSC-derived neurons. Scale bar, $2\,\mu m$. **k–m**, Four-week-old TD and WS iPSC-derived neurons show evoked action potentials (**k**), evoked voltage-dependent sodium and potassium currents (**l**) and spontaneous bursts of action potentials (**m**).

(Fig. 2f, g) and caspase-positive populations (Fig. 2h, i) in WS NPCs, indicating increased apoptosis.

FZD9 is expressed in NPCs[14] (Fig. 2j) and has been shown to regulate cell division and programmed cell death in different cell types[15,16]. In our study, *FZD9* was hemizygously deleted in the participants with typical WS, but retained in atypical pWS88 (Fig. 1a and Extended Data Fig. 1b). Thus, we hypothesized that *FZD9* regulates human NPC apoptosis. We transduced TD NPCs with a lentivirus carrying either short hairpin RNA (shRNA) against *FZD9* (shFZD9) or non-specific shRNA (shControl) and WS NPCs with lentiviruses carrying a *FZD9* cDNA construct (Fig. 2k, l). TD NPCs transduced with shFZD9 showed a reduction in the number of cells on day 4 (Fig. 2m) and an increase in the subG1 population (Fig. 2n) and caspase activity (Fig. 2o) compared with TD NPCs expressing the shControl. Similar results were observed in atypical pWS88 (Extended Data Fig. 4k–n). Restoring

FZD9 expression in typical WS NPCs brought the number of NPCs on day 4/day 0 to a similar level to TD NPCs. It also significantly reduced the apoptotic population to the TD level.

Since several Wnt genes were downregulated in WS NPCs (Extended Data Tables 2 and 3) and FZD9 can be activated by Wnt ligands, we tested if we could rescue the NPC viability by treating cells with the GSK3 inhibitor CHIR98014 (ref. 17). First, we confirmed that the canonical Wnt pathway was affected in WS by measuring the Axin2 and SP5 expression levels, two universal Wnt target genes[18,19]. Both genes were significantly downregulated in WS cells compared with TDs (Fig. 2p, q). By treating WS NPCs with CHIR98014, we were able to rescue cell viability (Fig. 2r). Together, our results indicate a role for FZD9 in NPC viability.

Our protocol generated a consistent population of forebrain neurons, confirmed by the pan-neuronal and subtype-specific cortical markers
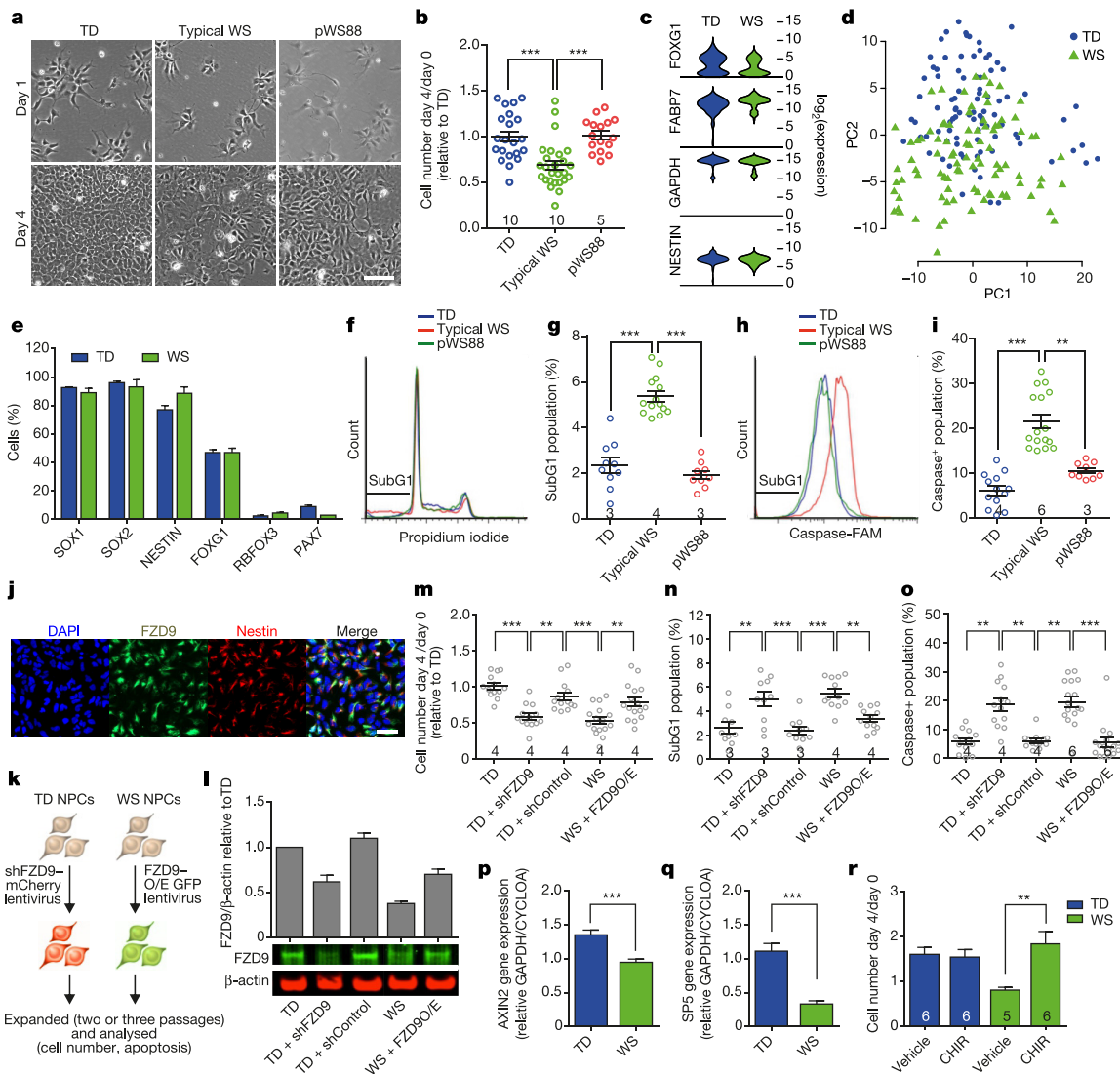
Figure 2 | Defect in apoptosis of WS-derived NPCs owing to haploinsufficiency of *FZD9*. a, Representative images showing the difference in confluency between TD, typical WS and pWS88 iPSC-derived NPCs on day 4. Scale bar, 100 μm. **b**, Ratio of NPC number on day 4 over day 0 relative to TD. **c**, Violin plots of representative genes expressed in NPCs from single-cell analyses. **d**, Principal component analysis (PCA) was used to compare the expression levels in individual cells on the basis of the first two principal components. **e**, Percentage of cells expressing NPC, neuronal (*RBFOX3*) and neural crest (*PAX7*, contaminant population) related genes. WS and TD iPSC-derived NPCs show similar percentages of cells expressing target genes over defined cycle threshold (C_t) control values. **f**, Representative propidium iodide histogram showing an increase in subG1 population in typical WS NPCs. **g**, Percentage of subG1 population. **h**, Representative histogram showing an increase in caspase activity (caspase-FAM intensity) in typical WS NPCs. **i**, Percentage of population with high caspase activity. **j**, FZD9 protein expression in TD iPSC-derived NPCs. **k**, Schematic of *FZD9* gain/loss of function experiments in NPCs. **l**, Expression level of FZD9 protein after treatment with shFZD9, shControl and *FZD9* overexpression vectors, assessed by western blot analysis. **m–o**, Ratio of NPC number on day 4 over day 0 relative to TD (**m**), percentage of subG1 population (**n**) and percentage of population with high caspase activity (**o**) when TD NPCs were treated with shFZD9 and shControl, and WS NPCs were overexpressed with *FZD9*. **p–q**, Significant decrease in expression of Axin2 (**p**) and SP5 (**q**) of WS NPCs compared with TDs. **r**, Rescue of WS NPC viability after CHIR98014 treatment. All data are shown as mean ± s.e.m.; *n*, number of clones. **$P < 0.01$, ***$P < 0.001$, Kruskal–Wallis test and Dunn's multiple comparison test (**b**, **g**, **i**), one-way ANOVA and Tukey's post hoc test (**g**, **m–o**), two-sided unpaired Student's *t* test (**p**, **q**), two-sided unpaired Mann–Whitney test (**r**).

such as *CTIP2* (layers V/VI)[20–22] and *SATB2* (layer III) (Fig. 1h, i). The neuronal population was also characterized by single-cell gene expression profiling (Fig. 3a–c and Extended Data Fig. 5a–f), revealing mostly glutamatergic neurons, with a small population of GABAergic (γ-aminobutyric-acid-releasing) neurons and glia (Fig. 3a). We did not detect significant variability in these subtypes of neurons expressing target genes or in the expression levels of several markers for cortical layers and neurotransmitters among the genotypes. However, we did detect differences in the expression of specific genes in these populations (Fig. 3b, c) that could lead to specific alterations in mature neurons. We focused specifically on markers for cortical layers V/VI,

since pathologies affecting these layers have been reported in disorders with compromised social functioning, such as autism[23]. We found that typical WS iPSC-derived CTIP2-positive neurons had significantly higher total dendritic length, dendrite number and number of dendritic spines than TDs (Fig. 3d–g and Extended Data Fig. 6a–m). Interestingly, atypical pWS88 neurons were morphologically similar to TD neurons except for dendrite number (Fig. 3f). To determine whether the WS neuronal phenotype was cell autonomous or dependent on other cells or culture conditions, we recorded the dendritic growth over time. The result showed a faster dendritic growth rate in WS neurons compared with TD or pWS88 (Extended Data Fig. 6n–r).
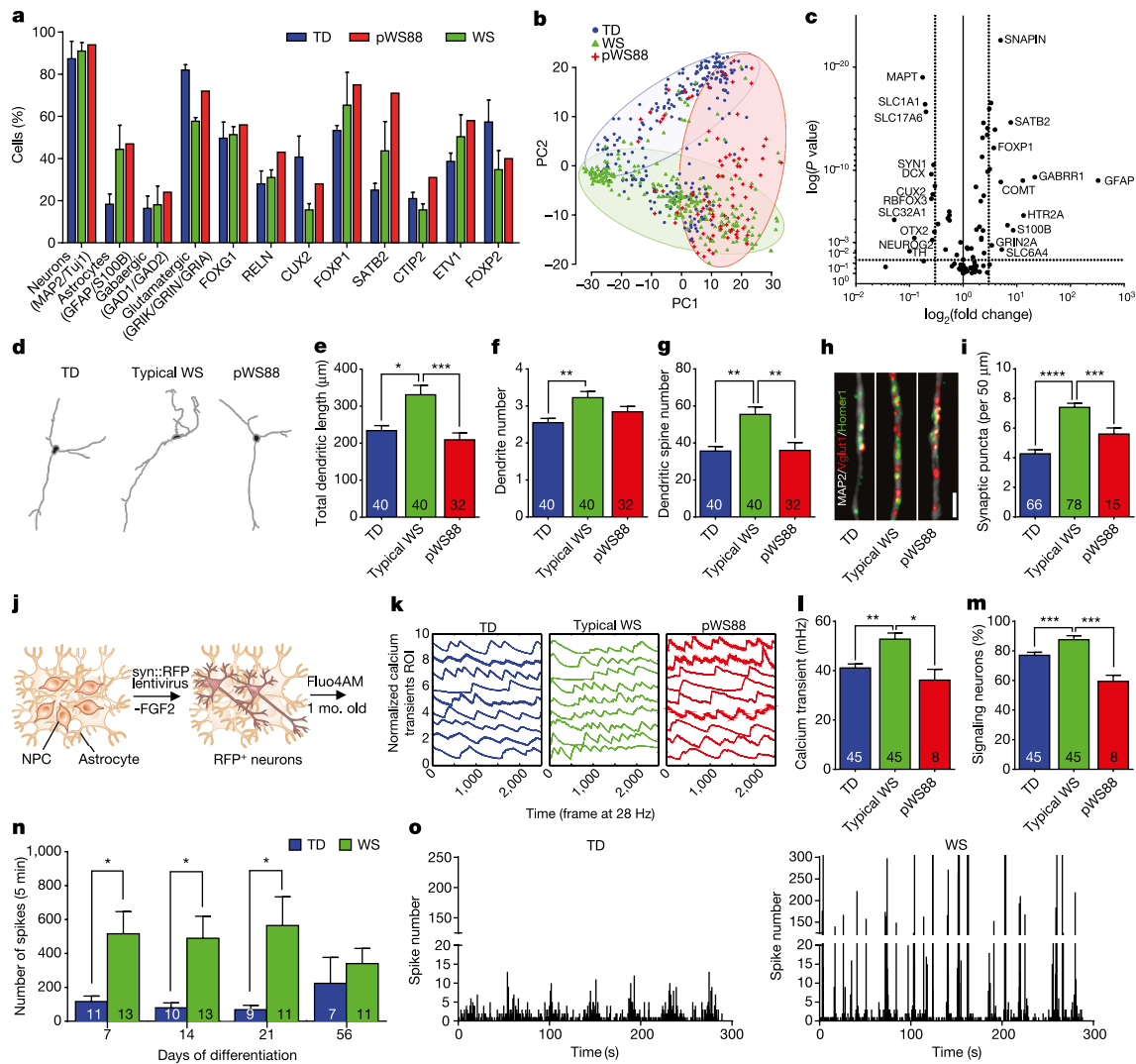
Figure 3 | Altered morphology of WS-derived cortical neurons and network activity. a, Percentage of cells expressing neural markers, neurotransmitter and cortical layer-related genes. WS, pWS88 and TD iPSC-derived neurons show non-significant percentage of cells expressing target genes over defined control C_t value. **b**, PCA of 672 cells projected onto the first two components. Overlaid populations of TD, pWS88 and WS neurons are shown. **c**, Volcano plot illustrates differences in expression patterns of target genes of iPSC-derived neurons from the single-cell analyses. The dotted lines represent more than or equal to 3.0-fold differentially expressed genes between the groups at $P < 0.05$ (unpaired Student's t test). **d**, Representative images of tracings from TD, typical WS and atypical pWS88 iPSC-derived neurons (Syn::EGFP- and CTIP2-positive neurons). **e–g**, Morphometric analyses showing significant differences between TD, typical WS and pWS88 in total dendritic length (**e**), between TD and typical WS in dendrite number (**f**) and between TD, typical WS and pWS88 in dendritic spine number (**g**). **h**, **i**, Puncta quantification of post- and presynaptic markers. Scale bar, 2 μm. For **e–g** and **i**, data are shown as mean ± s.e.m.; n, number of

traced neurons. $*P < 0.05$, $**P < 0.01$, $***P < 0.001$, $****P < 0.0001$, Kruskal–Wallis test and Dunn's multiple comparison test (**e–g**), one-way ANOVA and Tukey's post hoc test (**i**). **j**, Schematic diagram summarizing preparation of neurons for calcium transient analysis. **k**, Representative images of the calcium tracing from iPSC-derived neurons. Fluorescence intensity changes reflecting intracellular calcium fluctuations in neurons in different regions of interest (ROI). **l**, **m**, Typical WS-derived neurons exhibited significant increase in calcium transient frequency (**l**) and percentage of signalling neuron in the culture (**m**) when compared with TD or pWS88 neurons. Data are shown as mean ± s.e.m.; n, number of fields analysed; 3,198 neurons for TD, 4,446 neurons for WS and 48 neurons for pWS88. $*P < 0.05$, $**P < 0.01$, $***P < 0.001$, Kruskal–Wallis test and Dunn's multiple comparison test. **n**, MEA analyses revealed an increase in spontaneous neuronal spikes in WS during differentiation compared with TD. **o**, Although the number of total network bursts do not differ, WS shows a higher number of spikes in each burst compared with TD. Data are shown as mean ± s.e.m.; n, number of MEA wells analysed. $*P < 0.05$, $**P < 0.01$, two-sided unpaired Student's t test.

Also, no differences were observed in the total dendritic length, segment number or spine density using NPCs plated at different cellular densities (Extended Data Fig. 6 s–u).

An increase in the number of dendritic spines per neuron could lead to an increase in synaptic contacts and, therefore, synaptic activity[24], which could result in functional alterations. WS neurons had significantly more glutamatergic excitatory synapses compared with TD and pWS88 (Fig. 3h, i and Extended Data Figs 6v and 7a) and an increased frequency of calcium transients with a higher percentage of signalling neurons in WS cultures (Fig. 3j–m and Extended Data Fig. 7b–f). Using

multi-electrode array (MEA) electrophysiology, our data showed that WS neuronal cultures had a significant increase in spike frequency compared with TD-derived neurons (Fig. 3n, o and Extended Data Fig. 7g, h).

In an attempt to place our iPSC findings in the larger context of the cortical morphology of human participants at the gross anatomical and cellular levels, we conducted two sets of additional experiments to test predictions based on NPC and neuronal differences found *in vitro*. In addition to the total volume reduction in WS brains previously reported[25], multivariate analyses of variance (MANOVA) from
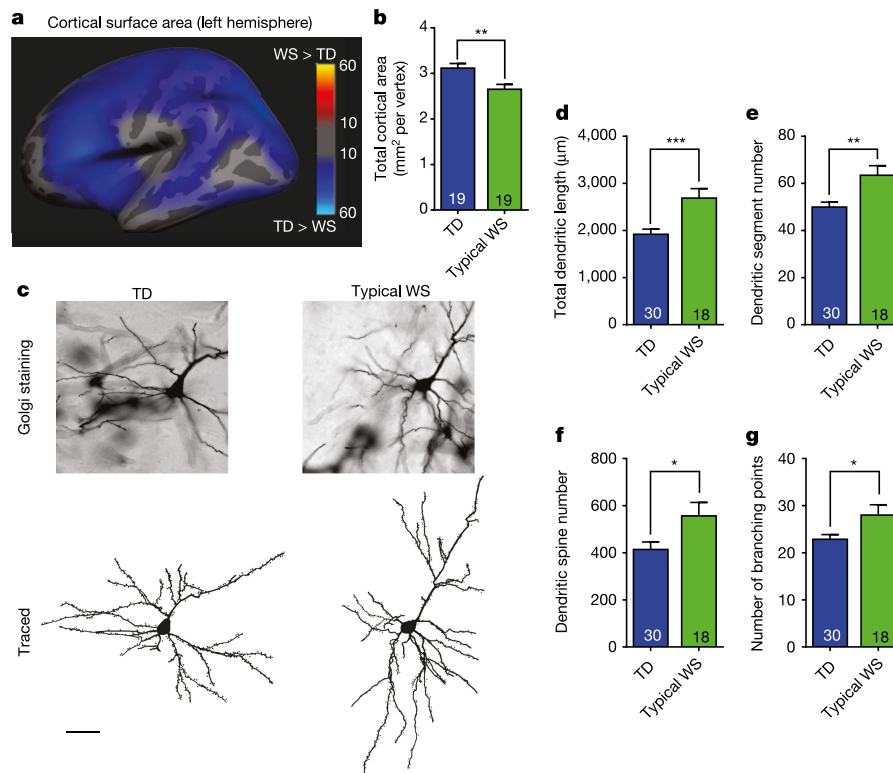
Figure 4 | Neuroanatomical and morphological alterations in WS human brains. a, Statistical parametric map of the vertex-wise group differences between TD and WS in cortical surface area (left hemisphere shown) assessed by structural MRI scans. Colour scales indicate the *P* value for statistical test: blue, decrease; grey, no difference. Statistics are displayed on a template group-averaged cortical surface rendering of TD adult participants. **b**, Reduction in overall cerebral cortical surface area in WS. Data are shown as mean ± s.e.m.; *n*, number of brains analysed. **P < 0.01, one-sided unpaired Student's *t* test. **c**, Representative images of post-mortem cortical layer V/VI pyramidal neurons using Golgi staining (top) and their corresponding tracing (bottom) from TD and WS. **d–g**, Morphometric analysis showing significant increases in total dendritic length (**d**), dendritic spine numbers (**e**), dendritic segment number (**f**) and number of branching points (**g**) in WS compared with TD post-mortem cortical layer V/VI pyramidal neurons. Data are shown as mean ± s.e.m.; *n*, number of traced neurons. *P < 0.05, **P < 0.01, ***P < 0.001, two-sided unpaired Student's *t* test (**d**), two-sided unpaired Mann–Whitney test (**e–g**).

our structural brain imaging of living participants revealed a significant decrease in overall cortical surface area in WS compared with TD individuals (Fig. 4a, b), but not in cortical thickness. Additionally, we conducted a separate set of experiments on post-mortem brains from WS and TD tissue donors to investigate possible alterations in the morphology of cortical neurons, as predicted by our iPSC findings. Similar to WS iPSC-derived CTIP2-positive neurons, post-mortem layer V/VI pyramidal neurons displayed larger total dendritic length and higher number of dendritic spines (Fig. 4c–e), and similar spine density and soma area, than TD neurons (Extended Data Fig. 7i–s). Post-mortem layer V/VI neurons also showed significantly increased numbers of dendritic segments and branching points (Fig. 4f, g), and similar numbers of dendritic trees.

The morphometric data in combination with the increased glutamatergic gene expression and number of co-localized synaptic puncta observed in neurons from WS suggest that an increased number of synapses may result in the altered network activity, which could contribute to the characteristic behaviour of individuals with WS. Our study reveals that the WS phenotypes described here are the foundation for the understanding of the complex human social behaviour. This approach provides an additional strategy to study the cellular and molecular underpinnings of complex human attributes, such as language in a social environment.

Online Content Methods, along with any additional Extended Data display items and Source Data, are available in the online version of the paper; references unique to these sections appear only in the online paper.

1. Korenberg, J. R. *et al.* VI. Genome structure and cognitive map of Williams syndrome. *J. Cogn. Neurosci.* **12** (Suppl. 1), 89–107 (2000).
2. Meyer-Lindenberg, A. *et al.* Neural basis of genetically determined visuospatial construction deficit in Williams syndrome. *Neuron* **43,** 623–631 (2004).
3. Bellugi, U., Lichtenberger, L., Mills, D., Galaburda, A. & Korenberg, J. R. Bridging cognition, the brain and molecular genetics: evidence from Williams syndrome. *Trends Neurosci.* **22,** 197–207 (1999).
4. Bellugi, U., Lichtenberger, L., Jones, W., Lai, Z. & St George, M. I. The neurocognitive profile of Williams syndrome: a complex pattern of strengths and weaknesses. *J. Cogn. Neurosci.* **12** (Suppl. 1), 7–29 (2000).
5. Doyle, T. F., Bellugi, U., Korenberg, J. R. & Graham, J. "Everybody in the world is my friend" hypersociability in young children with Williams syndrome. *Am. J. Med. Genet. A* **124,** 263–273 (2004).
6. Dai, L. *et al.* Is it Williams syndrome? GTF2IRD1 implicated in visual-spatial construction and GTF2I in sociability revealed by high resolution arrays. *Am. J. Med. Genet. A* **149A,** 302–314 (2009).
7. Edelmann, L. *et al.* An atypical deletion of the Williams–Beuren syndrome interval implicates genes associated with defective visuospatial processing and autism. *J. Med. Genet.* **44,** 136–143 (2007).
8. Chailangkarn, T., Acab, A. & Muotri, A. R. Modeling neurodevelopmental disorders using human neurons. *Curr. Opin. Neurobiol.* **22,** 785–790 (2012).
9. Ewart, A. K. *et al.* Hemizygosity at the elastin locus in a developmental disorder, Williams syndrome. *Nature Genet.* **5,** 11–16 (1993).
10. Järvinen-Pasley, A. *et al.* Defining the social phenotype in Williams syndrome: a model for linking gene, the brain, and behavior. *Dev. Psychopathol.* **20,** 1–35 (2008).
11. Marchetto, M. C. *et al.* A model for neural development and treatment of Rett syndrome using human induced pluripotent stem cells. *Cell* **143,** 527–539 (2010).
12. Beltrão-Braga, P. C. B. *et al.* Feeder-free derivation of induced pluripotent stem cells from human immature dental pulp stem cells. *Cell Transplant.* **20,** 1707–1719 (2011).
13. Adamo, A. *et al.* 7q11.23 dosage-dependent dysregulation in human pluripotent stem cells affects transcriptional programs in disease-relevant lineages. *Nature Genet.* **47,** 132–141 (2015).
14. Van Raay, T. J. *et al.* frizzled 9 is expressed in neural precursor cells in the developing neural tube. *Dev. Genes Evol.* **211,** 453–457 (2001).

15. Zhao, C. *et al.* Hippocampal and visuospatial learning defects in mice with a deletion of frizzled 9, a gene in the Williams syndrome deletion interval. *Development* **132**, 2917–2927 (2005).
16. Fujimoto, T., Tomizawa, M. & Yokosuka, O. SiRNA of frizzled-9 suppresses proliferation and motility of hepatoma cells. *Int. J. Oncol.* **35**, 861–866 (2009).
17. Lian, X. *et al.* Efficient differentiation of human pluripotent stem cells to endothelial progenitors via small-molecule activation of WNT signaling. *Stem Cell Rep.* **3**, 804–816 (2014).
18. Jho, E. H. *et al.* Wnt/beta-catenin/Tcf signaling induces the transcription of Axin2, a negative regulator of the signaling pathway. *Mol. Cell. Biol.* **22**, 1172–1183 (2002).
19. Fujimura, N. *et al.* Wnt-mediated down-regulation of Sp1 target genes by a transcriptional repressor Sp5. *J. Biol. Chem.* **282**, 1225–1237 (2007).
20. Srinivasan, K. *et al.* A network of genetic repression and derepression specifies projection fates in the developing neocortex. *Proc. Natl Acad. Sci. USA* **109**, 19071–19078 (2012).
21. Chen, B. *et al.* The Fezf2–Ctip2 genetic pathway regulates the fate choice of subcortical projection neurons in the developing cerebral cortex. *Proc. Natl Acad. Sci. USA* **105**, 11382–11387 (2008).
22. Leone, D. P., Srinivasan, K., Chen, B., Alcamo, E. & McConnell, S. K. The determination of projection neuron identity in the developing cerebral cortex. *Curr. Opin. Neurobiol.* **18**, 28–35 (2008).
23. Hutsler, J. J. & Zhang, H. Increased dendritic spine densities on cortical projection neurons in autism spectrum disorders. *Brain Res.* **1309**, 83–94 (2010).
24. Spitzer, N. C., Root, C. M. & Borodinsky, L. N. Orchestrating neuronal differentiation: patterns of Ca^{2+} spikes specify transmitter choice. *Trends Neurosci.* **27**, 415–421 (2004).
25. Chiang, M. C. *et al.* 3D pattern of brain abnormalities in Williams syndrome visualized using tensor-based morphometry. *Neuroimage* **36**, 1096–1109 (2007).

Supplementary Information is available in the online version of the paper.

Author Contributions A.R.M., T.C. and C.A.T. designed the experiments and wrote the manuscript with input from K.S. and all authors. T.C. processed DPCs, generated and characterized iPSCs, NPCs and neurons, and performed cell number, proliferation, and apoptosis experiments as well as *FZD9* knockdown and overexpression and statistical analysis. C.A.T. performed C1 single-cell analyses, synaptic quantification, calcium imaging, cell density experiments, live neuronal morphology analysis and statistical analysis. B.C.F. performed MEA recording, PCR for retrovirus silencing and Wnt pathway gene-expression analysis. B.C.F. and S.E.R. prepared astrocytes for co-culture experiments, NPC characterization by flow cytometry and CHIR 98014 experiments. K.S. designed all morphometry experiments with B.H.-M. and B.J., and co-wrote the manuscript to link the various levels of investigation from the whole-brain imaging findings to the cellular level. L.S. prepared Golgi staining for post-mortem neurons with help from K.L.H. and B.J. B.H.-M. obtained morphometric data on iPSC-derived neurons and post-mortem neurons. D.X.Y., M.C.M., C.A.T. and L.M. performed calcium transient experiments and statistical analysis. T.T.B. performed brain scan and statistical analysis with help from A.M.D. C.B. performed electrophysiological tests. M.D., W.W., P.L. and Y.M.S. performed neurocognitive and social tests. A.J., Y.M.S., and M.C.A. performed analyses and interpretation of social/neurocognitive tests. R.H.H. performed bioinformatics analysis. L.D. and J.R.K. confirmed deletion of all cells from participants with WS who donated them for reprogramming. E.H., U.B., F.H.G., K.S. and A.R.M. edited the manuscript for publication.

Author Information Reprints and permissions information is available at www.nature.com/reprints. The authors declare no competing financial interests. Readers are welcome to comment on the online version of the paper. Correspondence and requests for materials should be addressed to A.R.M. (muotri@ucsd.edu) or K.S. (ksemende@ucsd.edu).

METHODS

Participants for behavioural study and source of cells for reprogramming. The study protocols were approved by University of California San Diego and Salk Institute IRB/ESCRO committees (protocols 141223ZF and 95-0001, respectively). Four TD individuals (ages 8–19 years) and five individuals with WS (ages 8–14 years; Extended Data Fig. 1a) were included in the analysis: four of the latter group had typical WS gene deletions and one (pWS88) had a partial deletion in the WS region. Informed consents were obtained from all participants or their parents as appropriate. Genetic diagnosis of WS was established using fluorescent *in situ* hybridization probes for elastin (*ELN*), a gene consistently associated with the deletion in the typical WS region[1,9]. All of the participants with WS having confirmed genetic deletion exhibited the medical and clinical characteristics of the WS phenotype, including previously established cognitive, behavioural and physical features associated with the syndrome[4]. A diagnosis of WS was confirmed on the basis of the Diagnostic Score Sheet (DSS) for WS (American Academy of Paediatrics Committee on Genetics, 2001), with a particular focus on the cardiovascular abnormalities and the characteristic facial features associated with the *ELN* deletion. The scores for the participants were at the mean for WS (9) or higher, with the individual with partial deletion in the WS chromosomal region (pWS88) scoring lower than the individuals with typical WS deletion. Similarly, pWS88 reported fewer symptoms with connective tissue and growth, his cognitive scores were slightly higher than the typical individuals with WS, and he did not demonstrate the disparity between verbal and visual–spatial abilities typical of WS. However, pWS88 did display behavioural and developmental features consistent with WS, including developmental delay, over-friendliness and anxiousness.

Behavioural and neurocognitive tests. The participants were administered standard tests to quantify their non-verbal and verbal abilities, as well as versions of the WS cognitive and social profiles to capture the distinct pattern of strengths and weaknesses both within and across domains associated with the WS cognitive and social phenotype. Details of the tests and the measures tapping into the two profiles are presented in Extended Data Fig. 1. The WS cognitive profiles for the five participants with WS were constructed by calculating the log of predictive likelihood ratios under assumed normality for age-appropriate TD versus WS classifications on the basis of verbal and performance IQ (VIQ and PIQ), Beery Developmental Test of Visual-Motor Integration (VMI) and Peabody Picture Vocabulary Test (PPVT) standard scores, subject to availability. Predictive distributions were based on the published normative mean and s.d. for each of the tests employed, whereas for the WS classification the predictive distributions[26] were determined using data from $n = 81$ (VIQ and PIQ), $n = 56$ (VMI) and $n = 97$ (PPVT) participants in a broader WS sample (described in Extended Data Fig. 1d). A tobit model was used to estimate parameters for individuals with WS on the VMI owing to the presence of floor effects. The WS social profiles for the five participants with WS were constructed using measures of social approach behaviour, emotionality/empathy and language use.

Confirmation of WS deletion. Quantitative PCR was used to define the breakpoints of deleted regions in DNA isolated from iPSCs, or lymphoblast cell lines for participants with WS, with probes spanning from CALN1 to WBSCR16 and template DNA. Taqman expression assay probes detecting the WS region genes were designed and synthesized with sequences shown in Supplementary Table 11. RNase P (VIC) was used as control. Quantitative PCR was performed on the ABI PRISM 7900HT system and the results were analysed using SDS 3.2.

Cell collection, reprogramming and characterization. We avoided invasive sample collection methods such as skin biopsy or blood withdrawal by taking advantage of the natural loss of deciduous teeth as a source of somatic cells. We chose to reprogram dental pulp cells (DPCs) because these cells develop from the same set of early progenitors that generate neurons. Furthermore, the neurons derived from iPSCs generated from DPCs express higher levels of forebrain genes compared with those generated from skin fibroblast-derived iPSCs[27], serving the purpose of this study. Deciduous teeth were collected when they fell out and were shipped to our laboratory in DMEM 1× (Mediatech) with 4% Pen/Strep (Mediatech). Dental pulp was pulled out, washed in PBS with 4% Pen/Strep and incubated in 5% TrypLE (Gibco) for 15 min. Pulp was partly dissociated using needles and plated in culture medium (DMEM/F12 50:50, 15% FBS, 1%NEAA, 1% fungizone and 2% Pen/Strep). In 1–4 weeks, DPCs migrated out of the pulp and could be passaged and frozen as stock. DPCs in early passage (two to three) were reprogrammed using pMXs retroviruses expressing Yamanaka transcription factors (obtained from Addgene, Cambridge, Massachusetts)[12]. After 4 days, transduced DPCs were trypsinized, plated on mouse embryonic fibroblasts and cultured using human embryonic stem cell (hESC) medium. After manually picked and clonally expanded, feeder-free iPSCs were grown on matrigel-coated dishes (BD Bioscience, San Jose, California) with mTeSR1 (StemCell Technologies) or iDEAL[28].

Karyotyping. All G-banding karyotyping analyses were performed by Molecular Diagnostics Service (San Diego, California) and Children's Hospital Los Angeles (Los Angeles, California).

Genotyping. Two hundred nanograms of DNA were processed and hybridized to the Illumina Infinium Human Core Exome BeadChip following manufacturer's instructions. Illumina GenomeStudio V2011.1 with the Genotyping Module version 1.9.4 was used to normalize data and call genotypes using reference data provided by Illumina. Illumina's cnv Partition and gada R packages were used to automatically detect aberrant copy number region. In addition, the B Allele Frequency (BAF) and Log R Ratio (LRR) distributions were manually checked to determine additional CNVs not detected by the software. Sample identification/relatedness was assessed by comparing called genotypes for each sample. The absolute number of different genotypes was counted and the Euclidean distances were calculated to identify relatedness of the samples.

Teratoma assay. Dissociated iPSC colonies were centrifuged and resuspended in 1:1 matrigel and phosphate buffer saline solution. The cells were injected subcutaneously in nude mice. After 1–2 months, teratomas were dissected, fixed and sliced. Sections were stained with haematoxylin and eosin for further analysis. Protocols were previously approved by the University of California San Diego Institutional Animal Care and Use Committee.

Neural induction and neuronal differentiation. iPSCs were cultured on matrigel-coated dishes and fed daily with mTeSR for 7 days. On the next day, mTeSR was substituted by N2 medium (DMEM/F12 supplemented with 0.5× N2-Supplement (Life Technologies), 1 μM dorsomorphin (Tocris) and 1 μM SB431542 (Stemgent)) for 1–2 days. iPSC colonies were lifted off, cultured in suspension on the shaker (95 r.p.m. at 37 °C) for 8 days to form embryoid bodies and fed with N2 media. Embryoid bodies then were mechanically dissociated, plated on a matrigel-coated dish and fed with N2B27 medium (DMEM/F12 supplemented with 0.5× N2-Supplement, 0.5× B27-Supplement (Life Technologies), 1% penicillin/streptomycin and 20 ng/mL FGF-2). The emerging rosettes were picked manually, dissociated completely using accutase and plated on a poly-ornithine/laminin-coated plate. NPCs were expanded in N2B27 medium and fed every other day. To differentiate NPCs into neurons, FGF-2 was withdrawn from the N2B27 medium. NPCs and neurons were characterized for stage-specific markers by immunostaining and flow cytometry (NPCs only), expression profile by single-cell RT–PCR and RNA sequencing and electrophysiological property (neurons).

Total RNA extraction. Total RNA of DPCs, iPSCs, NPCs and neurons was extracted using TRIzol reagent (Life Technologies) according to the manufacturer's protocols. Contaminating DNA in RNA samples was removed using TURBO DNase (Life Technologies) according to the manufacturer's protocols. Quality and quantity of DNase-treated RNA were assessed using NanoDrop 1000 (Thermo Scientific).

PCR for exogenous retrovirus DNA silencing. RNA was extracted from iPSCs as previously described using Trizol reagent (Life Technologies). cDNA was generated from the RNA using SuperScript III protocol according to the manufacturer's instructions. PCR was performed using primers listed below at the following cycles: 94 °C for 10 min; 35 repeats of 94 °C for 30 s, 62 °C for 30 s and 72 °C for 1 min; and finally, 72 °C for 7 min. As a positive control, the pMX plasmid of the four vectors used on the reprogramming of the cells was placed along the samples as well as water as a negative template control for amplification. As an additional positive control for the endogenous genes, two hESC lines were used along with our iPSCs: H1 and HUES6 cells. Primers used were as follows. Endo-cMyc: forward, TTG AGG GGC ATC GTC GCG GGA; reverse, GCG TCC TGG GAA GGG AGA TCC. Endo-Klf4: forward, GAA ATT CGC CCG CTC CGA TGA; reverse, CTG TGT GTT TGC GGT AGT GCC. Endo-OCT3/4: forward, TCT TTC CAC CAG GCC CCC GGC TC; reverse, TGC GGG CGG ACA TGG GGA GAT CC. Endo-SOX2: forward, GCC GAG TGG AAA CTT TTG TCG; reverse, GGC AGC GTG TAC TTA TCC TTC T. Exo transgenes pMXs-TgUS: forward, GTG GTG GTA CGG GAA ATC AC. Exo-Oct4 pMXs-Oct3/4-TgDS: reverse, TAG CCA GGT TCG AGA ATC CA. Exo-Sox2 pMXs-Sox2-TgDS: reverse, GGT TCT CCT GGG CCA TCT TA. Exo-Klf4 pMXs-Klf4-TgDS: reverse, GGG AAG TCG CTT CAT GTG AG. Exo-c-Myc pMXs-c-Myc-TgDS: reverse, AGC AGC TCG AAT TTC TTC CA.

Embryoid body formation for pluripotency characterization. Partly dissociated iPSCs were re-suspended in embryoid body medium (DMEM/F12 medium, 1× N2 supplement and 1% FBS) and cultured on shaker (95 r.p.m.) at 37 °C. Medium was changed every 3–4 days. After 20 days, total RNA of embryoid bodies was extracted for further gene expression analyses by qPCR.

Mycoplasma testing. All tissue culture samples were routinely tested for mycoplasma by PCR. One millilitre of media supernatants (with no antibiotics or fungizone) was collected for all cell lines, spun down and resuspended in TE buffer. Ten microlitres of each sample were used in PCR reaction with the following primers: forward, GGC GAA TGG GTG AGT AAC; reverse, CGG ATA ACG CTT GCG ACC T. Any positive sample was immediately discarded.

Microarray. Three hundred nanograms of total extracted RNA from each sample were subjected to microarray by using the Affymatrix GeneChip one-cycle target labelling kit (Affymatrix, Santa Clara, California) according to the manufacturer's recommended protocols. The resultant biotinylated cRNA was fragmented and then hybridized to the GeneChip Human 1.0 ST Array (764,885 probes, 28,869 genes, 19,734 gene-level probe sets with putative full-length transcript support (GenBank and RefSeq)) on the basis of human genome, Hg18. Arrays were prepared at the University of California DNA Core Facility. Arrays were analysed by the Affy (Affymetrix pre-processing)[29] Bioconductor software package for microarray data. Data were then normalized by the RMA (robust multichip averaging) method to background-corrected and normalized probe levels to obtain a summary expression of normalized values for each probe set. Normalized microarray samples were then clustered by a hierarchical approach based on a matrix of distances. Normalized expression data were used to create a distance matrix that was calculated on the basis of Euclidean distance between the transcripts over a pair of samples representing a variation between two samples. Having the distances for all pairs of samples, a linkage method is used to cluster samples in a dendrogram by using calculated distances (sample expression similarities). This method also creates a heat map to graphically show the expression correlation between the samples.

Gene expression analyses by qPCR. RNA samples were reverse transcribed into cDNA using the Super Script III First Strand Synthesis System (Invitrogen, California) according to the manufacturer's instructions. Reactions were run on the Bio-Rad detection system using Sybr-green master mix (Bio-Rad). Primers were selected from Primerbank; validated database (http://pga.mgh.harvard.edu/primerbank/) and specificities were confirmed by melting curve analysis through a Bio-Rad detection system. Sequences of the primers are described in Supplementary Table 12. Quantitative analysis used the comparative threshold cycle method[30]. GAPDH was used as housekeeping gene. Each sample was run in triplicate.

RNA-seq and global gene expression analyses. The RNA-seq analyses were previously described by our group[31]. Briefly, RNAs were isolated using the RNeasy Mini kit (Qiagen). A total of 1,000 ng of RNA was used for library preparation using the Illumina TruSeq RNA Sample Preparation Kit. The RNAs were sequenced on Illumina HiSeq2000 with 50 bp paired-end reads, generating 50 million high-quality sequencing fragments per sample on average. For validation purposes of biological samples subjected to RNA-seq, hESC and iPSC data available from the literature were downloaded and used to compare with our sequenced cell lines. The two hESC lines used are available (HUES-6, referred as ES(HUES), SRR873630, http://www.ncbi.nlm.nih.gov/sra/SRX290739; and H1, referred to here as ES(H1)), SRR873631, http://www.ncbi.nlm.nih.gov/sra/SRX290740). The two human iPSC lines used are available under accession codes SRR873619 (referred to here as iPS(TD,1)) and SRR873620 (referred to here as iPS(TD,2)).

Gene ontology (GO) enrichment analysis. RNA-seq enrichment used WebGestalt[32] and Cytoscape[33] software plugins, considering only categories having statistical significance ($P < 0.05$). Genes tested for differential expression were used as the background for GO annotation and enrichment analysis.

NPC counting. NPCs were seeded onto poly-ornithine/laminin-coated six-well plates at a total number of 10^5 cells per well on day 0. Medium change was done on day 2. Cells were collected and counted on day 4.

NPC flow characterization. NPCs were resuspended, dissociated with accutase and fixed using fixation buffer (BioLegend) for 15 min followed by three PBS washes. The cell pellet was incubated and kept in Perm III buffer (BD Biosciences) at −20 °C until needed for the experiment. A total of 10^6 cells were incubated with antibodies Sox1 (PE), Sox2 (APC) or Nestin (PE) and Pax6 (APC) (Bd Biosciences) for 30 min and then washed three times before being resuspended for cell analyses. Cells were analysed in a plate reader mode using FACS Canto II machine (BD Biosciences).

Immunofluorescence staining. Cells were fixed in 4% paraformaldehyde for 10–20 min, washed with PBS three times (5 min each), permeabilized with 0.1% Triton X-100 for 15 min, incubated in blocking solution (2% BSA) for 1 h at room temperature and then in primary antibodies (goat anti-Nanog, Abcam ab77095, 1:500; rabbit anti-Lin28, Abcam ab46020, 1:500; rabbit anti-Oct4, Abcam ab19857, 1:500; mouse anti-SSEA4, Abcam ab16287, 1:200; mouse anti-Nestin, Abcam ab22035, 1:200; rabbit anti-Musashi1, Abcam ab52865, 1:250; rat anti-CTIP2, Abcam ab18465, 1:250; rabbit anti-SATB2, Abcam ab34735, 1:200; chicken anti-MAP2, Abcam ab5392, 1:1,000; rabbit anti-FZD9, Origene TA314730, 1:150; chicken anti-EGFP, Abcam ab13970, 1:1,000; rabbit anti-Synapsin1, EMD-Millipore AB1543P, 1:500; mouse anti-Vglut1, Synaptic Systems 135311, 1:500; rabbit anti-Homer1, Synaptic Systems 160003, 1:500) overnight at 4 °C. The next day, cells were washed with PBS three times (5 min each), incubated with secondary antibodies (Alexa Fluor 488, 555 and 647, Life Technologies, 1:1,000) for 1 h at room temperature and washed with PBS three times (5 min each). Nuclei were

stained using DAPI (1:10,000). Slides or coverslips were mounted using ProLong Gold antifade mountant (Life Technologies).

DNA fragmentation analysis. One million NPCs were harvested to single-cell suspension in 1 mL PBS, then fixed by addition of 3 mL of 100% ethanol and stored at 4 °C for at least 2 h. NPC pellets were washed once with 5 mL PBS. After removal of PBS, cells were resuspended in 1 mL of propidium iodide (PI) staining solution (0.1% (v/v) Triton X-100, 10 μg/mL PI and 100 μg/mL RNase A in 1 × PBS). WS and TD NPC samples were analysed by FACS on a Becton Dickinson LSRI, and gating of subG1 population (cells with fragmented DNA) was examined using FlowJo flow cytometry analysis software.

Caspase assay. Caspase activity was measured using a Green FLICA Caspases 3 & 7 Assay Kit (ImmunoChemistry Technologies). Briefly, NPCs were harvested, washed and stained with 1 × carboxyfluorescein Fluorochrome Inhibitor of Caspase Assay (FAM-FLICA) reagent, 10 μg/mL Hoechst and 10 μg/mL propidium iodide (PI). Samples were analysed on the NC-3000 using the pre-optimized Caspase Assay. The population with caspase activity was used to analyse for apoptosis.

Proliferation assay. NPC proliferation was assessed using BD Pharmingen BrdU Flow Kits (BD Biosciences) according to the manufacturer's protocol. Briefly, NPCs were incubated with 1 μM BrdU for 45 min at 37 °C and harvested to single-cell suspension. NPCs were then fixed and permeabilized using BD Cytofix/Cytoperm Buffer and stained using FITC-conjugated anti-BrdU antibody and 7-aminoactinomycin D (7-AAD), a fluorescent dye for labelling DNA. Fluorescence-activated cell sorting (FACS) was done on LSRFortessa (BD Biosciences) and, to obtain the percentage of the BrdU-positive population, the cell-cycle profiles were analysed using FlowJo flow cytometry analysis software.

Construction and characterization of lentiviruses. Commercially available lentiviral vectors (pLKO.1) expressing short hairpin RNAs (shRNAs) against FZD9 under the control of the U6 promoter (Thermo Scientific) were engineered to express the *Discosoma* sp. red fluorescent protein (RFP) mCherry under the control of the hPGK (human phosphoglycerate kinase) promoter. The following shRNAs against *FZD9* and a non-silencing scrambled control shRNA were selected (Thermo Scientific): shRNA-control, 5′-TTC TCC GAA CGT GTC ACG T-3′; shRNA-FZD9, 5′-ATC TTG CGG ATG TGG AAG AGG-3′. For rescue experiments, FZD9 cDNA was amplified from TD NPC cDNA as template by the following primer pair: 5′-CCG AGA TCT TCG AGG TGT GTG GGG TTC TCC AAA G-3′; 5′-TCT AGA GCC ACC ATG GCC GTA GCG CCT CTG-3′.

The reaction was performed using Phusion High-Fidelity DNA polymerase (New England Biolabs) according to the manufacturer's protocol. The FZD9 cDNA was cloned into a lentiviral vector driven by the ubiquitin promoter followed by a self-cleavage peptide and GFP sequence. The specificity and efficiency of shRNA-control, shRNA-FZD9, and the FZD9-WT constructs were verified by co-transfection into HEK-293 cells. Cell lysates were collected and analysed by western blot analysis with anti-FZD9 antibodies (Aviva OAEC02415, 1:1,000).

CHIR-98014 treatment. CHIR-98014 (Selleckchem) was resuspended according to manufacturer's instructions into 10 mM stock using DMSO and then diluted to 100 μM. Final concentration used in cells was 100 nM of CHIR-98014, whereas the vehicle cells received only DMSO. For qPCR experiments, NPCs were propagated in six-well plates until 70% confluency and then treated with CHIR-98014 for 6 h to have their RNA collected using Trizol as previously described. For the NPC counting experiment, cells were seeded in six-well plates as described in the presence of CHIR-98014 or DMSO, in triplicates (TD and WS). After 48 h, the culture medium was changed and treatment was repeated. Cells were collected and counted after 96 h of incubation.

Astrocyte differentiation. The TD NPCs were lifted into suspension and maintained on a shaker (95 r.p.m.) to form neurospheres for 3 weeks. For the first week, the spheres were grown with N2B27 medium. The neurospheres were overlaid with the astrocyte medium (Lonza) for the remaining 2 weeks. The neurospheres were plated onto poly-ornithine- and laminin-coated plates and expanded for two to three passages before experimentation. Co-cultures of neurons and astrocytes were prepared for morphometric and functional analyses.

Western blotting. NPCs were lysed in RIPA buffer with protease inhibitor. Rabbit anti-FZD9 antibody (Aviva OAEC02415, 1:1,000) and mouse anti-β-actin (Abcam ab8226, 1:3,000) were used as primary antibodies. IRDye 800CW goat anti-rabbit and IRDye 680RD goat anti-mouse (1:10,000) were used as secondary antibodies. The Odyssey system was used for signal detection. Signal intensities were measured using the Odyssey Image Studio and semi- quantitative analysis of FZD9 signal intensity was corrected with respect to β-actin relative quantification. A paired t-test analysis with $P < 0.05$ was used in the comparison of TD and WS FZD9 signal intensity normalized data.

Synaptic puncta quantification. Co-localized Vglut (presynaptic) and Homer1 (postsynaptic) puncta were quantified after three-dimensional reconstruction of

z-stack random images for all individuals and from two different experiments. Slides were analysed under a fluorescence microscope (Z1 Axio Observer Apotome, Zeiss). Only puncta in proximity of MAP2-positive processes were scored.

Single-cell qRT–PCR and analysis. Specific target amplification was performed in individual dissociated NPCs or 6-week-old neurons using C1 Single-Cell and BioMark HD Systems (Fluidigm), according to the manufacturer's protocol and as described previously[34–36]. Briefly, single cells were captured on a C1 chip (10- to 17-μm cells) and cell viability was checked using a LIVE/DEAD Cell Viability/Cytotoxicity kit (Life Technologies). After lysis, RNA was reverse transcribed into cDNA with validated amplicon-specific DELTAgene Assays (Supplementary Table 13) using SuperScript III RT Platinum Taq Mix. Specific target amplification was performed by 18 cycles of 95 °C denaturation for 15 s and 60 °C annealing and amplification for 4 min. Each preamplified cDNA was mixed with 2× SsoFast EvaGreen Supermix with Low ROX (Bio-Rad) and then pipetted into an individual sample inlet in a 96.96 Dynamic Array IFC chip (Fluidigm). DELTAgene primer pairs (Supplementary Table 13) were diluted and pipetted into individual assay inlets in the same 96.96 Dynamic Array IFC chip. Quantitative PCR results were analysed using Fluidigm's Real-time PCR Analysis software using the linear (derivative) baseline correction method and the automatic (gene) C_t threshold method with 0.65 curve quality threshold. Hierarchical clustering heat map, PCA analyses, violin plots of $\log_2$(expression of C_t values) (limit of detection = 24) and ANOVA statistical analysis were performed using Singular Analysis Toolset 3.0 (Fluidigm).

Calcium imaging. Neuronal networks derived from human iPSCs were transduced with lentivirus carrying the Syn::RFP reporter construct. Cell cultures were washed with Krebs HEPES buffer (KHB) (10 mM HEPES, 4.2 mM NaHCO₃, 10 mM dextrose, 1.18 mM MgSO₄, 1.18 mM KH₂PO₄, 4.69 mM KCl, 118 mM NaCl, 1.29 mM NaCl₂; pH 7.3) and incubated with 2–5 μM Fluo-4AM (Molecular Probes/Invitrogen, Carlsbad, California) in KHB for 40 min. Five thousand frames were acquired at 28 Hz with a region of 256 pixels × 256 pixels (×100 magnification), using a Hamamatsu ORCA-ER digital camera (Hamamatsu Photonics K.K., Japan) with a 488 nm (FITC) filter on an Olympus IX81 inverted fluorescence confocal microscope (Olympus Optical, Japan). Images were acquired with MetaMorph 7.7 (MDS Analytical Technologies, Sunnyvale, California), processed and analysed using individual circular regions of interest (ROI) on ImageJ and Matlab 7.2 (Mathworks, Natick, Massachusetts). Syn::RFP⁺ neurons were selected after confirmation that calcium transients were blocked with 1 mM of tetrodotoxin (TTX). The amplitude of signals was presented as relative fluorescence changes (Δ*F*/*F*) after background subtraction. The threshold for calcium spikes was set at the 95th percentile of the amplitude of all detected events.

Electrophysiology. For whole-cell patch-clamp recordings, individual coverslips containing live 1-month-old neurons were transferred into a heated recording chamber and continuously perfused (1 mL/min) with artificial cerebrospinal fluid bubbled with a mixture of CO₂ (5%) and O₂ (95%) and maintained at 25 °C. Artificial cerebrospinal fluid contained (in mM) 121 NaCl, 4.2 KCl, 1.1 CaCl2, 1 MgSO₄, 29 NaHCO₃, 0.45 NaH₂PO₄-H₂O, 0.5 Na₂HPO₄ and 20 glucose (all chemicals from Sigma). Whole-cell recordings were performed using a digidata 1440A/ Multiclamp 700B and Clampex 10.3 (Molecular devices). Patch electrodes were filled with internal solutions containing 130 mM K-gluconate, 6 mM KCl, 4 mM NaCl, 10 mM Na-HEPES, 0.2 mM K-EGTA; 0.3 mM GTP, 2 mM Mg-ATP, 0.2 mM cAMP, 10 mM D-glucose, 0.15% biocytin and 0.06% rhodamine. The pH and osmolarity were adjusted for physiological conditions. Data were all corrected for liquid junction potentials, electrode capacitances were compensated on-line in cell-attached mode and a low-pass filter at 2 kHz was used. The access resistance of the cells in our sample was around 37 MΩ with resistance of the patch pipettes 3–5 MΩ. Spontaneous synaptic AMPA events were recorded at the reversal potential of Cl⁻ and could be reversibly blocked by AMPA receptor antagonist (10 μM NBQX, Sigma). Spontaneous synaptic GABA events were recorded at the reversal potential of Na⁺ and could be reversibly blocked with GABA_A receptor antagonist (10 μM SR95531, Sigma).

Multi-electrode array (MEA). Using 12-well MEA plates from Axion Biosystems, we plated the same density of NPCs from TD and WS individuals in triplicate. Each well was seeded with 10,000 NPCs that were induced into neuronal differentiation as previously described. Each well was coated with poly-L-ornithine and laminin before cell seeding. Cells were fed once a week and measurements were taken before the medium was changed. Recordings were performed using a Maestro MEA system and AxIS software (Axion Biosystems), using a band-pass filter with 10 Hz and 2.5 kHz cutoff frequencies. Spike detection was performed using an adaptive threshold set to 5.5 times the standard deviation of the estimated noise on each electrode. Each plate first rested for 5 min in the Maestro, and then 5–10 min of data were recorded to calculate the spike rate per well. MEA analysis was performed using the Axion Biosystems Neural Metrics Tool,

wherein electrodes that detected at least five spikes per minute were classified as active electrodes. Bursts were identified in the data recorded from each individual electrode using an adaptive Poisson surprise algorithm. Network bursts were identified for each well, using a non-adaptive algorithm requiring a minimum of ten spikes with a maximum inter-spike interval of 100 ms. Only channels that exhibited bursting activity (more than ten spikes in 5 min interval) were included in this analysis. After measurement, neurons were immunostained to check morphology and density.

Post-mortem brain specimens and cortical sampling. We used six post-mortem brains (two WS and four TD) that were gender-, age- and hemisphere-matched. All brain specimens were harvested within a post-mortem interval of 18–30 h and had been immersed and fixed in 10% formalin for up to 20 years. For the purpose of the present experiments, samples were obtained from anatomically well-identified cortical areas in a consistent manner across specimens. Tissue blocks approximately 5 mm³ were removed from primary somatosensory cortex (Brodmann area 3) and primary motor cortex (Brodmann area 4) in the arm/hand knob region of the pre- and postcentral gyri, respectively, and from the secondary visual area (Brodmann area 18) from approximately 1.4 cm dorsally to the occipital pole and 2 cm from the midline[37,38]. We focused specifically on these parts of the cortex because pathologies in dendritic morphology in these areas have been reported in other neurodevelopmental disorders[39–41]. In addition, pyramidal neurons in the selected areas reach their mature-like morphology early in development and start displaying dendritic pathologies sooner than high integration areas, such as the prefrontal cortex, allowing comparison of post-mortem findings with iPSC-derived neurons in early stages of development[42,43].

Post-mortem brain tissue processing. Sampled tissue blocks were processed using an adaptation of the Golgi–Kopsch method[44], which has been shown to give good results with tissue that has been fixed for long periods[45]. Briefly, blocks were immersed in a solution of 3% potassium dichromate, 0.5% formalin for 8 days, followed by immersion into 0.75% silver nitrate for 2 days. Blocks were then sectioned on a vibratome, perpendicular to the pial surface, at a thickness of 120 μm. Golgi sections were cut into 100% ethyl alcohol and transferred briefly into methyl salicylate followed by toluene, mounted onto glass slides and coverslipped. Adjacent blocks from each region were sectioned at 60 μm and stained with thionin for visualization of cell bodies and laminar organization, which enabled identification of the position of each neuron within a specific cortical layer. Cytoarchitectonic analysis of histological sections from each block confirmed that tissue was sampled from the ROI and that the Golgi-impregnated pyramidal neurons were located in cortical layers V/VI.

Morphometric analysis of Golgi-impregnated neurons. Cortical neurons from all six post-mortem brains were used in the study. Neurons included in the morphological analysis did not display degenerative changes[46]. Only neurons with fully impregnated soma, apical dendrites with present oblique branches and at least two basal dendrites with third-order segments were chosen for the analysis[47]. To minimize the effects of cutting on dendritic measurements, we included neurons with cell bodies located near the centre of 120-μm-thick histological sections, with natural terminations of higher-order dendritic branches present where possible[37,47]. Inclusion of the neurons completely contained within 120-μm sections biases the sample towards smaller dendrites, leading to the underestimation of dendritic length[48]; therefore, we applied the same criteria blinded across all WS and TD specimens, and we thus included the neurons with incomplete endings if they were judged to otherwise fulfil the criteria for successful Golgi impregnation. All neurons were oriented with apical dendrite perpendicular to the pial surface; inverted pyramidal cells as well as magnopyramidal neurons were excluded from the analysis. Neuronal morphology was quantified along *x*-, *y*-, and *z*-coordinates using Neurolucida version 10 software (MBF Bioscience, Williston, Vermont) connected to a Nikon Eclipse 80i microscope, with a ×40 (0.75 numerical aperture) Plan Fluor dry objective. Tracings were conducted on both apical and basal dendrites, and the results reflect summed values for both types of dendrite per neuron. Following the recommendation that the applications of Sholl's concentric spheres or Eayrs' concentric circles for the analysis of neuronal morphology are not adequate when neuronal morphology is analysed in three dimensions[48], we conducted dendritic tree analysis with the following measurements[37,47]: (1) soma area—cross sectional surface area of the cell body; (2) dendritic length—summed total length of all dendrites per neuron; (3) dendrite number—number of dendritic trees emerging directly from the soma per neuron; (4) dendritic segment number—total number of segments per neuron; (5) dendritic spine/protrusion number—total number of dendritic spines per neuron; (6) dendritic spine/protrusion density—average number of spines per 20 μm of dendritic length; and (7) branching point number—number of nodes (points at the dendrite where a dendrite branches into two or more) per neuron. Dendritic segments were defined as parts of the dendrites between two branching points—between the soma and the first branching point

in the case of first-order dendritic segments, and between the last branching point and the termination of the dendrite in the case of terminal dendritic segments. Since the long formalin-fixation time could have resulted in degradation of dendritic spines, spine values might be underestimated and are thus reported here with caution. All of the tracings were accomplished blind to brain region and diagnostic status.

Morphometric analysis of iPSC-derived neurons. The iPSC-derived sample consisted of EGFP-positive 8-week-old neurons with pyramidal- or ovoid-shaped soma and at least two branched neurites (dendrites) with visible spines/protrusions. Protrusions from dendritic shaft, which morphologically resembled dendritic spines in post-mortem specimens, were considered and quantified as dendritic spines in iPSC-derived neurons. The neurites were considered dendrites on the basis of the criteria applied in post-mortem studies: (1) thickness that decreased with the distance from the cell body; (2) branches emerging under acute angle; and (3) presence of dendritic spines. In addition, only enhanced-GFP-positive neurons with nuclei co-stained with CTIP2, indicative of layer V/VI neurons, and with the dendrites displaying evenly distributed fluorescent stain along their entire length, were included in the analysis. The morphology of the neurons was quantified along x-, y-, and z-coordinates using Neurolucida version 9 software (MBF Bioscience, Williston, VT) connected to a Nikon Eclipse E600 microscope with a $\times 40$ oil objective. No distinction was made between apical and basal dendrites, and the results reflect summed length values of all neurites/dendrites per neuron, consistent with what was done for the post-mortem neurons. The same set of measurements used in the analysis of Golgi-impregnated neurons was applied to the analysis of iPSC-derived neurons, and all of the tracings were accomplished blind to the diagnostic status and were conducted by the same rater (B.H.-M.). Intra-rater reliability was assessed by having the rater trace the same neuron after a period of time. The average coefficient of variation between the results of retraced neurons was 2% for soma area (SA), total dendritic length (TDL), dendritic segment number (DSN) and branching point number (BPN), and 3% for dendritic spine/protrusion number (DPN); there was no variation in tree/dendrite number (TN) in different tracings of the same neuron. The accuracy was further checked by having three individuals (B.H.-M., B.J. and L.S.) trace the same neuron.

Brain imaging data acquisition and quality control. MRI scanning was completed in 19 participants with WS (aged 19–43 years; mean 29.0, s.d. 8.8; 11 males, 8 females) and 19 TD comparison participants (aged 16–43 years; mean 26.2, s.d. 7.3; 8 males, 11 females). There was no significant difference between the groups in age ($t = 1.0$, $P < 0.30$) or in gender ratio (Pearson's $\chi^2 = 0.95$, $P < 0.33$). A standardized multiple modality high-resolution structural MRI protocol was implemented, involving three-dimensional T_1- and T_2-weighted volumes and a set of diffusion-weighted scans. Imaging data were obtained at the University of California San Diego Radiology Imaging Laboratory on a 1.5 T GE Signa HDx 14.0M5 TwinSpeed system (GE Healthcare, Waukesha, Wisconsin) using an eight-channel phased array head coil. A three-dimensional inversion recovery spoiled gradient echo (IR-SPGR) T_1-weighted volume was acquired with pulse sequence parameters optimized for maximum grey/white matter contrast (echo time = 3.9 ms, repetition time = 8.7 ms, inversion time = 270 ms, flip angle = 8°, difference in echo times = 750 ms, bandwidth = ± 15.63 kHz, field of view = 24 cm, matrix = 192 × 192, voxel size = 1.25 mm × 1.25 mm × 1.2 mm). All MRI data were collected using prospective motion (PROMO) correction for non-diffusion imaging[49]. This method has been shown to improve image quality, reduce motion-related artefacts, increase the reliability of quantitative measures and improve the clinical diagnostic utility of MRI data obtained in children and clinical groups[50,51]. Standardized quality control procedures were followed for both raw and processed data, including visual inspection ratings by a trained imaging technician and computer algorithms testing general image characteristics as well as aspects specific to each imaging modality, such as contrast properties, registrations and artefacts from motion and other sources. Participants included in the current analyses were only those who passed all raw and processed quality control measures.
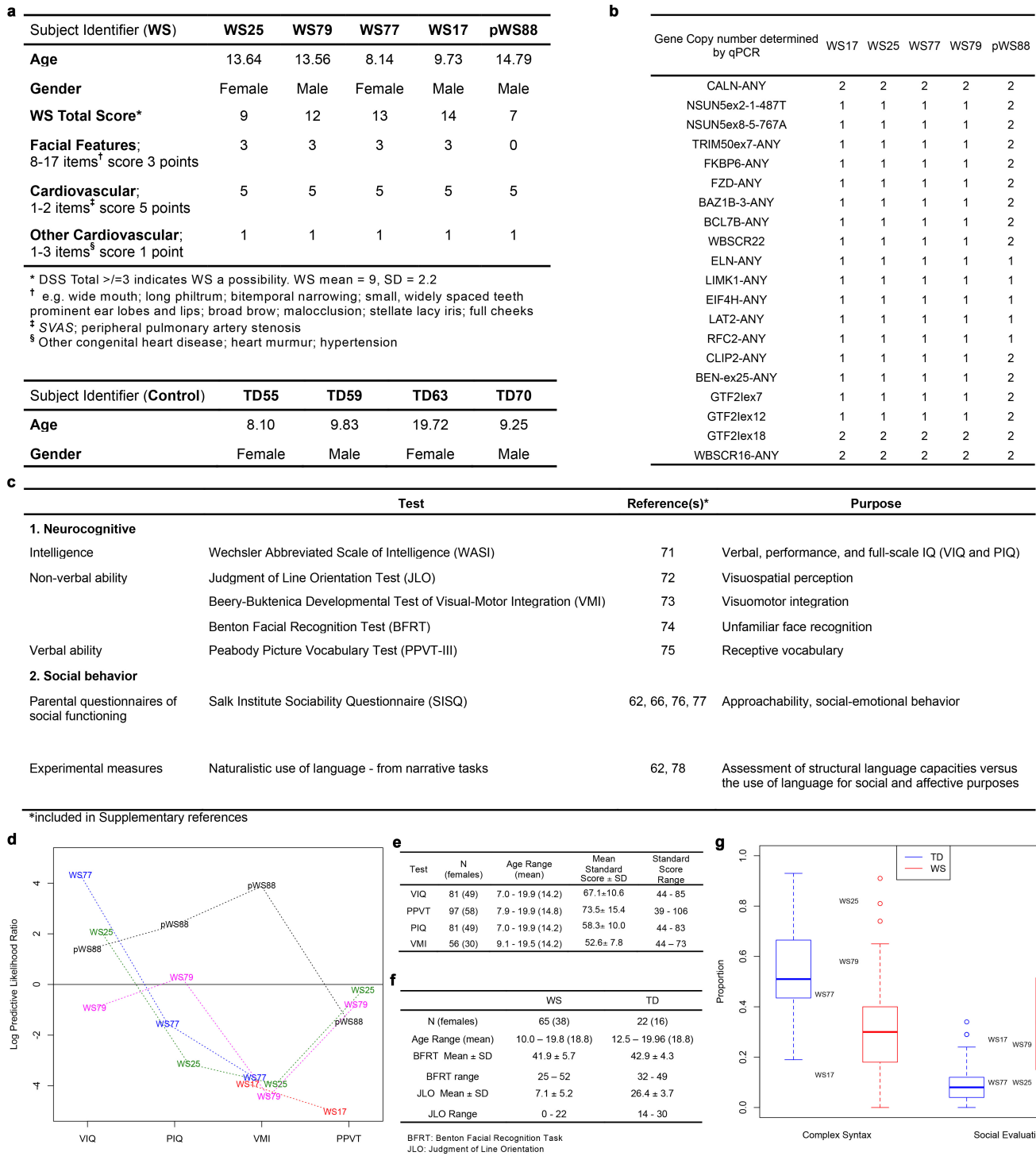
MRI data post-processing. Image post-processing and analysis were performed using FreeSurfer software suite (http://surfer.nmr.mgh.harvard.edu/). Surface-based cortical reconstruction and subcortical volumetric segmentation procedures have been shown elsewhere[52–58]. Briefly, a three-dimensional model of the cortical surface was generated using MRI scans with four attributes: white matter segmentation; tessellation of the grey/white matter boundary; inflation of the folded, tessellated surface; and correction of topological defects[53,54]. Cortical thickness was measured using the distances from each point on the white matter surface to the pial surface[57]. Cortical surface area was measured at the pial surface for the entire cerebrum and for each parcel of the Desikan and Destrieux atlases[53,54,58,59].

Statistical analysis. Means ± s.e.m. for each parameter were obtained from samples described in Supplementary Table 1. There were no statistical methods used to predetermine sample size. The experiments were not randomized. All of the tracings were accomplished blind to brain region and diagnostic status. All statistical analyses were done using Prism (Graphpad). Before statistical analysis comparing means between between three to five unmatched groups of data, normal distribution was tested using D'Agostino and Pearson omnibus normality test and variance similarity was tested using Bartlett's test for equal variances. Means of three to five unmatched groups, where normal distribution and equal variances between groups were confirmed, were statistically compared using one-way ANOVA and Tukey's post hoc test. Otherwise, a Kruskal–Wallis test and Dunn's multiple comparison test were used. Before statistical analysis comparing means between two unmatched groups of data, normal distribution was tested using D'Agostino and Pearson omnibus normality test and variance similarity was tested using an F test to compare variances. To compare the means of two groups where normal distribution and similar variance between groups were confirmed, Student's t test was used. Otherwise, a Mann–Whitney test was used. Significance was defined as $*P < 0.05$, $**P < 0.01$, $***P < 0.001$ or $****P < 0.0001$.

26. Lawless, J. F. & Fredette, M. Frequentist prediction intervals and predictive distributions. *Biometrika* **92**, 529–542 (2005).
27. Chen, J. *et al.* Transcriptome comparison of human neurons generated using induced pluripotent stem cells derived from dental pulp and skin fibroblasts. *PLoS ONE* **8**, e75682 (2013).
28. Marinho, P. A., Chailangkarn, T. & Muotri, A. R. Systematic optimization of human pluripotent stem cells media using Design of Experiments. *Sci. Rep.* **5**, 9834 (2015).
29. Gautier, L., Cope, L., Bolstad, B. M. & Irizarry, R. A. affy—analysis of *Affymetrix GeneChip* data at the probe level. *Bioinformatics* **20**, 307–315 (2004).
30. Livak, K. J. & Schmittgen, T. D. Analysis of relative gene expression data using real-time quantitative PCR and the $2^{-\Delta\Delta C_T}$ method. *Methods* **25**, 402–408 (2001).
31. Marchetto, M. C. *et al.* Differential L1 regulation in pluripotent stem cells of humans and apes. *Nature* **503**, 525–529 (2013).
32. Zhang, B., Kirov, S. & Snoddy, J. WebGestalt: an integrated system for exploring gene sets in various biological contexts. *Nucleic Acids Res.* **33**, W741–W748 (2005).
33. Shannon, P. *et al.* Cytoscape: a software environment for integrated models of biomolecular interaction networks. *Genome Res.* **13**, 2498–2504 (2003).
34. Llorens-Bobadilla, E. *et al.* Single-cell transcriptomics reveals a population of dormant neural stem cells that become activated upon brain injury. *Cell Stem Cell* **17**, 329–340 (2015).
35. Livak, K. J. *et al.* Methods for qPCR gene expression profiling applied to 1440 lymphoblastoid single cells. *Methods* **59**, 71–79 (2013).
36. Hermann, B. P. *et al.* Transcriptional and translational heterogeneity among neonatal mouse spermatogonia. *Biol. Reprod.* **92**, 54 (2015).
37. Jacobs, B. *et al.* Regional dendritic and spine variation in human cerebral cortex: a quantitative golgi study. *Cereb. Cortex* **11**, 558–571 (2001).
38. Semendeferi, K. *et al.* Spatial organization of neurons in the frontal pole sets humans apart from great apes. *Cereb. Cortex* **21**, 1485–1497 (2011).
39. Marin-Padilla, M. Structural abnormalities of the cerebral cortex in human chromosomal aberrations: a Golgi study. *Brain Res.* **44**, 625–629 (1972).
40. Takashima, S., Becker, L. E., Armstrong, D. L. & Chan, F. Abnormal neuronal development in the visual cortex of the human fetus and infant with down's syndrome. A quantitative and qualitative Golgi study. *Brain Res.* **225**, 1–21 (1981).
41. Jay, V., Chan, F. W. & Becker, L. E. Dendritic arborization in the human fetus and infant with the trisomy 18 syndrome. *Brain Res. Dev. Brain Res.* **54**, 291–294 (1990).
42. Marin-Padilla, M. Prenatal and early postnatal ontogenesis of the human motor cortex: a golgi study. II. The basket-pyramidal system. *Brain Res.* **23**, 185–191 (1970).
43. Vukšić, M., Petanjek, Z., Rasin, M. R. & Kostović, I. Perinatal growth of prefrontal layer III pyramids in Down syndrome. *Pediatr. Neurol.* **27**, 36–38 (2002).
44. Jacobs, B. *et al.* Quantitative analysis of cortical pyramidal neurons after corpus callosotomy. *Ann. Neurol.* **54**, 126–130 (2003).
45. Riley, J. N. A reliable Golgi-Kopsch modification. *Brain Res. Bull.* **4**, 127–129 (1979).
46. Williams, R. S., Ferrante, R. J. & Caviness, V. S., Jr. The Golgi rapid method in clinical neuropathology: the morphologic consequences of suboptimal fixation. *J. Neuropathol. Exp. Neurol.* **37**, 13–33 (1978).
47. Jacobs, B. & Scheibel, A. B. A quantitative dendritic analysis of Wernicke's area in humans. I. Lifespan changes. *J. Comp. Neurol.* **327**, 83–96 (1993).
48. Uylings, H. B., Ruiz-Marcos, A. & van Pelt, J. The metric analysis of three-dimensional dendritic tree patterns: a methodological review. *J. Neurosci. Methods* **18**, 127–151 (1986).
49. White, N. *et al.* PROMO: Real-time prospective motion correction in MRI using image-based tracking. *Magn. Reson. Med.* **63**, 91–105 (2010).
50. Brown, T. T. *et al.* Prospective motion correction of high-resolution magnetic resonance imaging data in children. *Neuroimage* **53**, 139–145 (2010).
51. Kuperman, J. M. *et al.* Prospective motion correction improves diagnostic utility of pediatric MRI scans. *Pediatr. Radiol.* **41**, 1578–1582 (2011).

52. Jovicich, J. *et al.* Reliability in multi-site structural MRI studies: effects of gradient non-linearity correction on phantom and human data. *Neuroimage* **30,** 436–443 (2006).
53. Dale, A. M., Fischl, B. & Sereno, M. I. Cortical surface-based analysis. I. Segmentation and surface reconstruction. *Neuroimage* **9,** 179–194 (1999).
54. Fischl, B., Sereno, M. I. & Dale, A. M. Cortical surface-based analysis. II: Inflation, flattening, and a surface-based coordinate system. *Neuroimage* **9,** 195–207 (1999).
55. Fischl, B. *et al.* Sequence-independent segmentation of magnetic resonance images. *Neuroimage* **23** (Suppl 1), S69–S84 (2004).
56. Fischl, B. *et al.* Automatically parcellating the human cerebral cortex. *Cereb. Cortex* **14,** 11–22 (2004).
57. Fischl, B. & Dale, A. M. Measuring the thickness of the human cerebral cortex from magnetic resonance images. *Proc. Natl Acad. Sci. USA* **97,** 11050–11055 (2000).
58. Desikan, R. S. *et al.* An automated labeling system for subdividing the human cerebral cortex on MRI scans into gyral based regions of interest. *Neuroimage* **31,** 968–980 (2006).
59. Destrieux, C., Fischl, B., Dale, A. & Halgren, E. Automatic parcellation of human cortical gyri and sulci using standard anatomical nomenclature. *Neuroimage* **53,** 1–15 (2010).

a

Subject Identifier (**WS**)	**WS25**	**WS79**	**WS77**	**WS17**	**pWS88**
Age	13.64	13.56	8.14	9.73	14.79
Gender	Female	Male	Female	Male	Male
WS Total Score*	9	12	13	14	7
Facial Features; 8-17 items[†] score 3 points	3	3	3	3	0
Cardiovascular; 1-2 items[‡] score 5 points	5	5	5	5	5
Other Cardiovascular; 1-3 items[§] score 1 point	1	1	1	1	1

* DSS Total >/=3 indicates WS a possibility. WS mean = 9, SD = 2.2
[†] e.g. wide mouth; long philtrum; bitemporal narrowing; small, widely spaced teeth prominent ear lobes and lips; broad brow; malocclusion; stellate lacy iris; full cheeks
[‡] *SVAS*; peripheral pulmonary artery stenosis
[§] Other congenital heart disease; heart murmur; hypertension

Subject Identifier (**Control**)	**TD55**	**TD59**	**TD63**	**TD70**
Age	8.10	9.83	19.72	9.25
Gender	Female	Male	Female	Male

b

Gene Copy number determined by qPCR	WS17	WS25	WS77	WS79	pWS88
CALN-ANY	2	2	2	2	2
NSUN5ex2-1-487T	1	1	1	1	2
NSUN5ex8-5-767A	1	1	1	1	2
TRIM50ex7-ANY	1	1	1	1	2
FKBP6-ANY	1	1	1	1	2
FZD-ANY	1	1	1	1	2
BAZ1B-3-ANY	1	1	1	1	2
BCL7B-ANY	1	1	1	1	2
WBSCR22	1	1	1	1	2
ELN-ANY	1	1	1	1	1
LIMK1-ANY	1	1	1	1	1
EIF4H-ANY	1	1	1	1	1
LAT2-ANY	1	1	1	1	1
RFC2-ANY	1	1	1	1	1
CLIP2-ANY	1	1	1	1	2
BEN-ex25-ANY	1	1	1	1	2
GTF2Iex7	1	1	1	1	2
GTF2Iex12	1	1	1	1	2
GTF2Iex18	2	2	2	2	2
WBSCR16-ANY	2	2	2	2	2

c

	Test	Reference(s)*	Purpose
1. Neurocognitive			
Intelligence	Wechsler Abbreviated Scale of Intelligence (WASI)	71	Verbal, performance, and full-scale IQ (VIQ and PIQ)
Non-verbal ability	Judgment of Line Orientation Test (JLO)	72	Visuospatial perception
	Beery-Buktenica Developmental Test of Visual-Motor Integration (VMI)	73	Visuomotor integration
	Benton Facial Recognition Test (BFRT)	74	Unfamiliar face recognition
Verbal ability	Peabody Picture Vocabulary Test (PPVT-III)	75	Receptive vocabulary
2. Social behavior			
Parental questionnaires of social functioning	Salk Institute Sociability Questionnaire (SISQ)	62, 66, 76, 77	Approachability, social-emotional behavior
Experimental measures	Naturalistic use of language - from narrative tasks	62, 78	Assessment of structural language capacities versus the use of language for social and affective purposes

*included in Supplementary references

d

e

Test	N (females)	Age Range (mean)	Mean Standard Score ± SD	Standard Score Range
VIQ	81 (49)	7.0 - 19.9 (14.2)	67.1± 10.6	44 - 85
PPVT	97 (58)	7.9 - 19.9 (14.8)	73.5± 15.4	39 - 106
PIQ	81 (49)	7.0 - 19.9 (14.2)	58.3± 10.0	44 - 83
VMI	56 (30)	9.1 - 19.5 (14.2)	52.6± 7.8	44 – 73

f

	WS	TD
N (females)	65 (38)	22 (16)
Age Range (mean)	10.0 – 19.8 (18.8)	12.5 – 19.96 (18.8)
BFRT Mean ± SD	41.9 ± 5.7	42.9 ± 4.3
BFRT range	25 – 52	32 - 49
JLO Mean ± SD	7.1 ± 5.2	26.4 ± 3.7
JLO Range	0 - 22	14 - 30

BFRT: Benton Facial Recognition Task
JLO: Judgment of Line Orientation

g

Extended Data Figure 1 | Participants with WS in iPSC study and their neurocognitive and social profiles. a, Summary of scores on the Diagnostic Score Sheet (DSS) for individuals with WS. **b**, Table showing allele number of genes in WS-deleted region in each participant obtained from qPCR. **c**, Summary of all neurocognitive and social behavioural tests used on this study. **d**, **e**, WS neurocognitive profiles. Log of predictive likelihood ratio for iPSC participants (identified by participant number) calculated as the log of the ratio of the likelihoods for each individual test score based on the predictive distributions for TD individuals and those with WS (**d**). Values less than 0 indicate depressed scores consistent with expectations for WS. Predictive distributions for TD participants used published norms (means and standard deviations with assumed normality). Predictive distributions for individuals with WS were calculated using available WS data (VIQ/PIQ $n = 81$, VMI $n = 56$, PPVT $n = 97$) (**e**), assuming normality and least squares estimation, and according to the procedures described elsewhere[26]. WS parameter estimates for the VMI were calculated using censored regression owing to several individuals with WS scoring at the instrument floor. **f**, Description of population included in Benton Face Recognition and Judgment of Line Orientation in Fig. 1b (TD $n = 22$ versus WS $n = 65$). **g**, Boxplots for WS (red) and TD (blue) participants on complex syntax (WS $n = 45$; TD $n = 47$) and social evaluation (WS $n = 44$; TD $n = 49$). Red and blue circles depict scores more than 1.5 times the interquartile range away from the median.
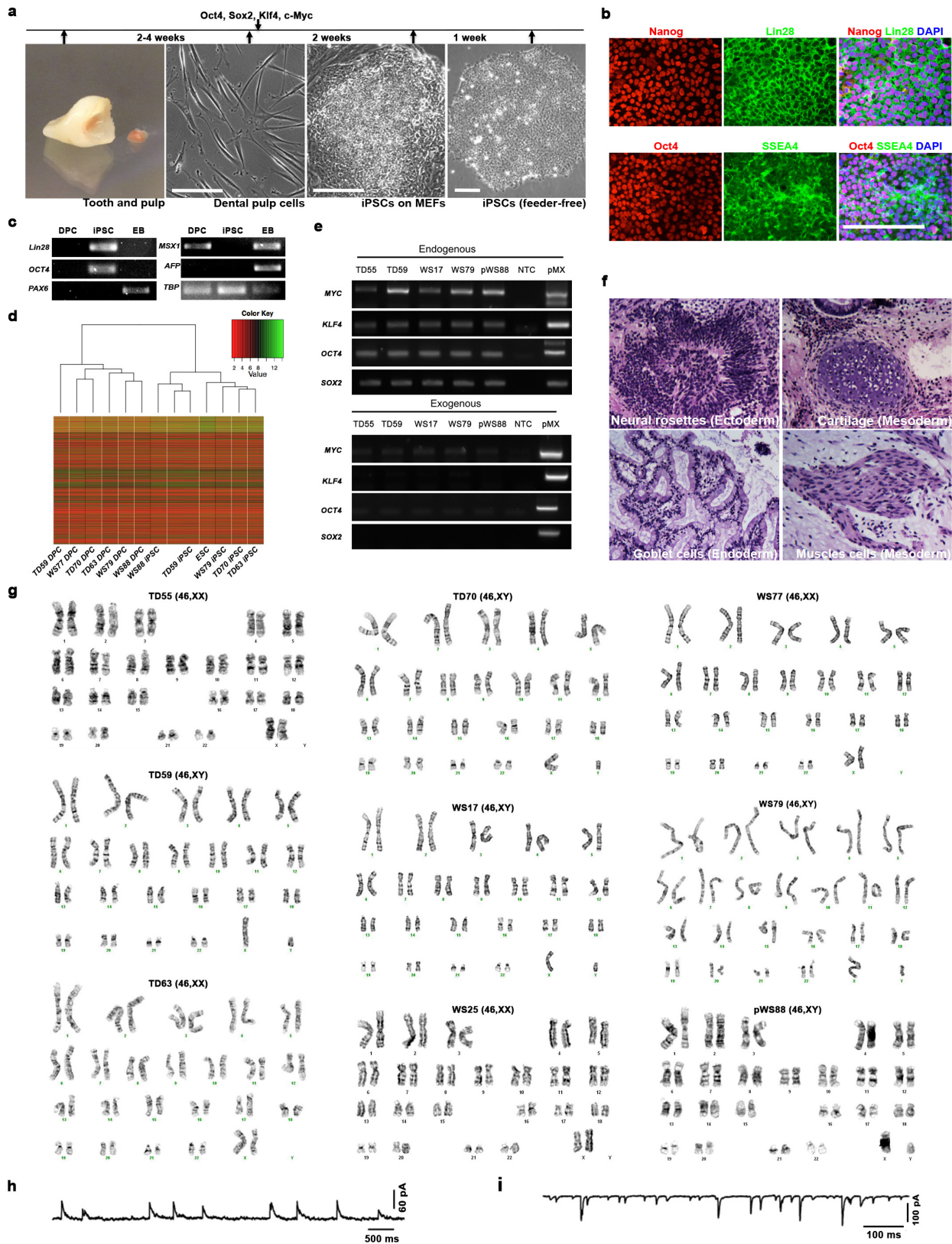
Extended Data Figure 2 | Generation and characterization of iPSCs.
a, Summary of reprogramming protocol using retrovirus carrying Yamanaka transcription factors (see Supplementary Information for details). Scale bar, 200 μm. **b**, Representative images of iPSCs expressing pluripotent markers including Nanog, Lin28, Oct4 and SSEA4 assessed by immunofluorescence staining. Scale bar, 200 μm. **c**, Expression of three germ-layer markers in iPSC-derived embryoid bodies (EBs); *PAX6* (ectoderm), *MSX1* (mesoderm) and *AFP* (endoderm) assessed by semiquantitative RT–PCR. *TBP*, housekeeping control. **d**, Cluster analysis showing correlation coefficients of microarray profiles of three

WS DPCs, three TD DPCs, three WS iPSCs, three TD iPSCs and one ESC. **e**, Representative PCR showing silencing of the four transgenes (exogenous) in iPSCs. **f**, Representative images of teratoma from iPSCs showing tissues of three germ layers; neural rosettes (ectoderm), cartilage (mesoderm), muscle cells (mesoderm) and goblet cells (endoderm). **g**, Representative image of iPSC chromosomes showing its genetic stability assessed by G-banding karyotype analysis. **h**, **i**, Spontaneous synaptic GABA events (**h**) and spontaneous synaptic AMPA events (**i**) in 1-month-old iPSC-derived neurons.
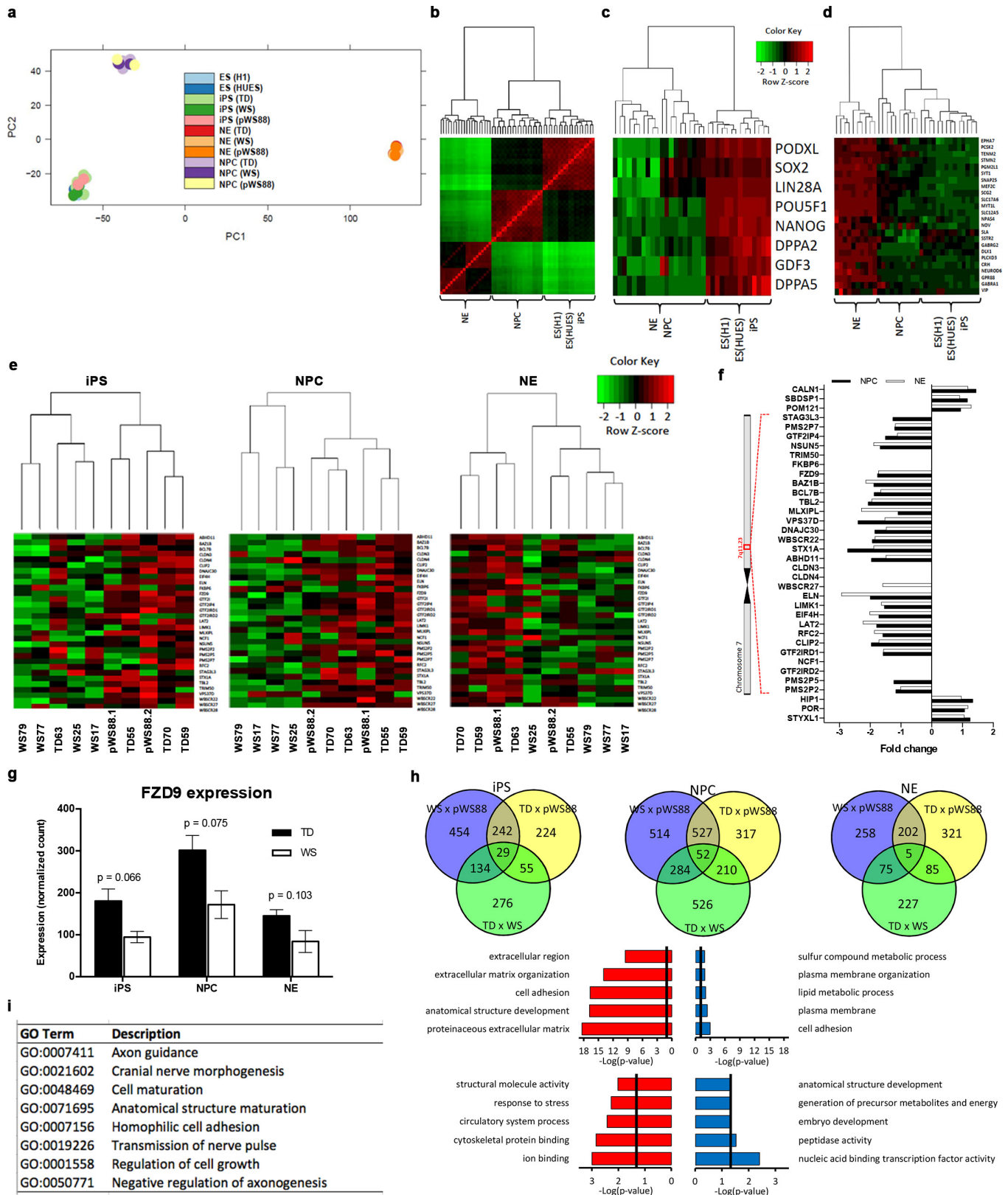
Extended Data Figure 3 | See next page for caption.

Extended Data Figure 3 | Global gene expression analysis during neuronal differentiation. a, PCA plot of embryonic stem cells (ES), induced pluripotent stem cells (iPS), neuronal progenitor cells (NPC) and neurons (NE) for TD, WS and pWS88. **c**, Euclidian matrix distance-based heat map and hierarchical clustering-based dendrogram of ES, NPC and NE cells for WD, WS and pWS88 samples. Expression variability between samples is indicated by Z-score, varying from green (negative variation) to red (positive variation). **c**, Euclidian matrix distance-based heat map and hierarchical clustering-based dendrogram of pluripotency gene markers for ES, NPC and NE cells for TD, WS and pWS88 samples. **d**, Euclidian matrix distance-based heat map and hierarchical clustering-based dendrogram of neuronal gene markers for iPS, NPC and NE cells for TD, WS and pWS88 samples. Expression variability between samples is indicated by Z-score, varying from green (negative variation) to red (positive variation). **e**, Specific cell type-based clustering analysis of biological replicates subjected to RNA-seq for the WS-related genes in three stages during differentiation (iPS, NPC and NE). **f**, Fold change variation of WS-related genes in different cell lines. Ideogram of chromosome 7 (band 7q11.23) corresponding to the commonly deleted region with the WS-related genes. Fold change variation of normalized WS-related gene expression in NPCs and neurons (NE) compared with TDs. Non-represented fold change corresponds to those genes having high expression variability between biological replicates, or having very low expression values. **g**, Expression of *FZD9* gene in iPSC, NPCs and neurons from TD and WS. Error bars, s.e.m. **h**, Venn diagram showing correlation of significant differentially expressed genes between TD, pWS88 and WS during neuronal differentiation. Significantly enriched GO terms found for downregulated (red histogram) and upregulated (blue histogram) differentially expressed genes between TD and WS in NPC. Significantly enriched GO terms found for downregulated (red histogram) and upregulated (blue histogram) differentially expressed genes between TD and WS in neurons (NE). Vertical line (black) corresponds to a significant *P* value (<0.05). **i**, Enriched GO metabolic process terms found in NPC of WS samples correlated with the GO found by a similar comparison performed in ref. 13.
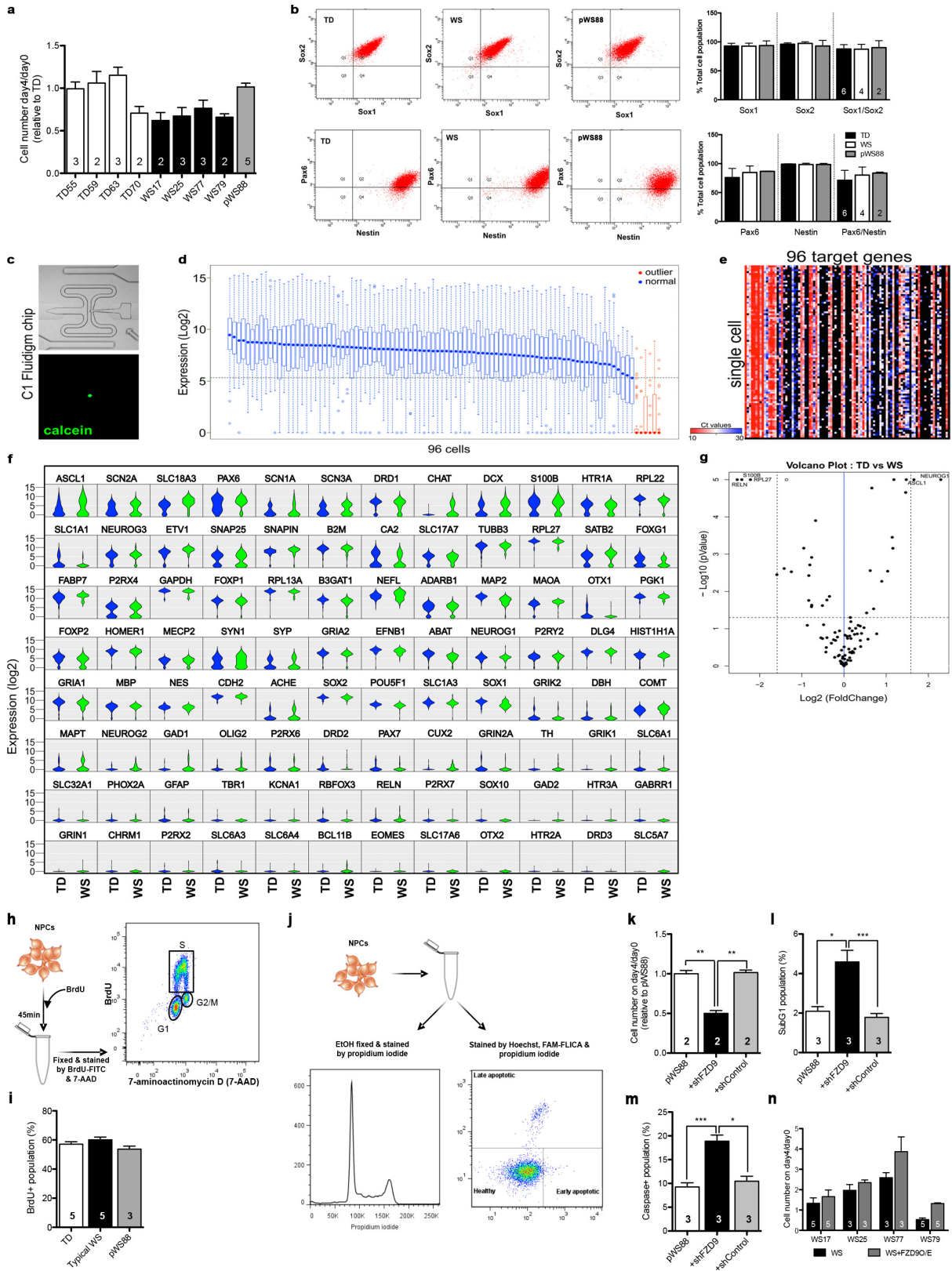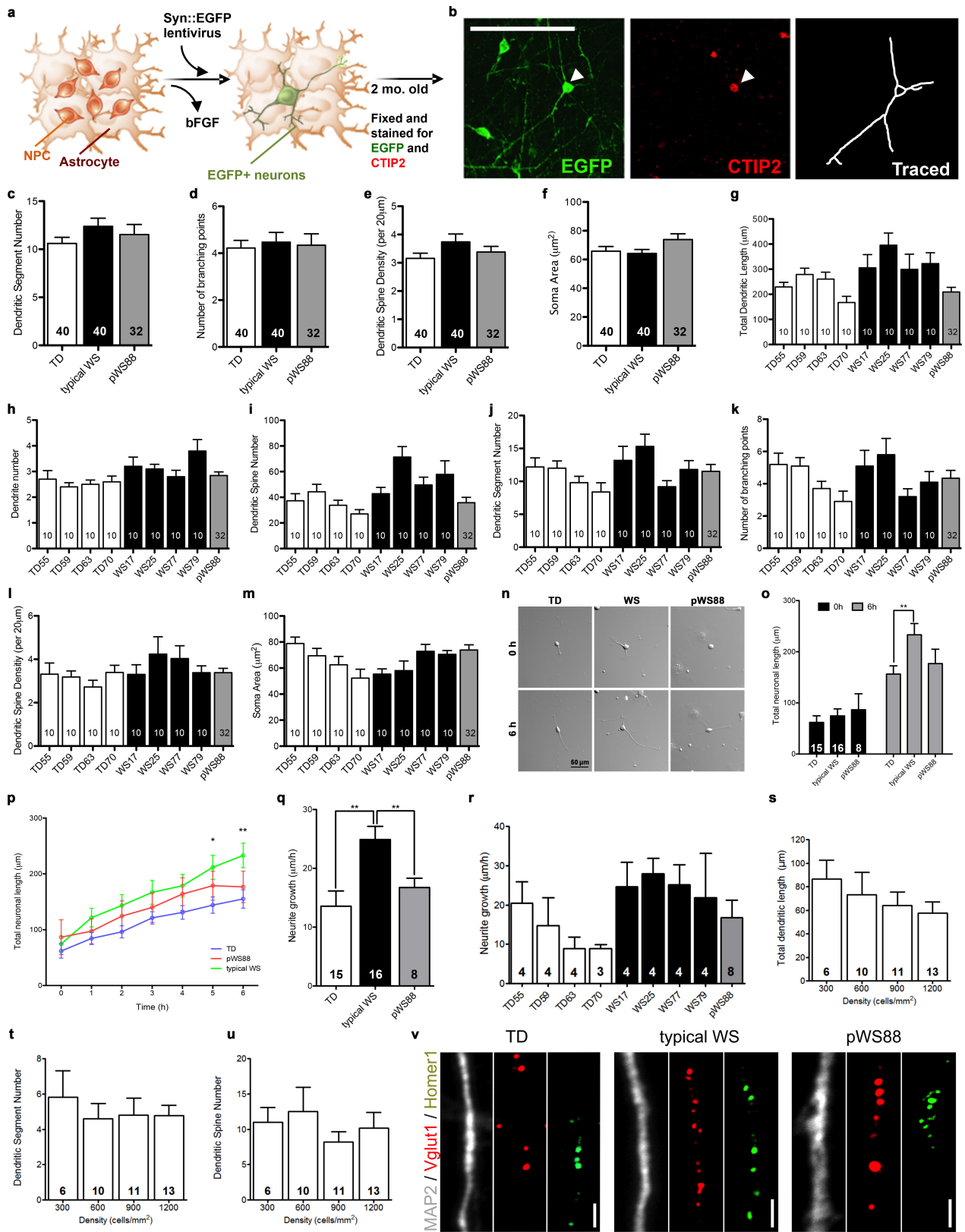
Extended Data Figure 4 | See next page for caption.

Extended Data Figure 4 | Defect in WS NPC apoptosis and role of FZD9. a, Ratio of NPC number on day 4 over day 0 relative to TD. Data are shown as mean $\pm$ s.e.m.; n, number of clones. **b**, High percentage ($>$95%) of Sox1/Sox2-positive and Pax6/Nestin-positive cell population was comparably observed in TD, typical WS and pWS88 NPCs assessed by FACS. Data are shown as mean $\pm$ s.e.m.; n, number of clones. **c**, Microfluidics of C1 chip used to capture live single cells (calcein$^+$ cell). **d**, Outlier exclusion based on the recommended/default limit of detection value of 24, analysed by Fluidigm Singular 3.0. Outliers were removed manually on the basis of the sample median $\log_2$(expression) values. **e**, Representative example of non-normalized C_t plot, indicated with the rectangle in the heat map. Cells are shown in rows and genes in columns. The range of cycle threshold (C_t) values is colour coded from low (blue) to high (red) and absent (black). **f**, Violin plots of all 96 genes showing the comparison between TD and WS NPCs from the single-cell analyses ($\log_2$(expression) values). The majority of genes show unimodal expression distribution. **g**, Volcano plot of single-cell expression data. Plot illustrates differences in expression patterns of target genes of

iPSC-derived NPCs. The dotted lines represent more than or equal to 3.0-fold differentially expressed genes between the groups at $P < 0.05$ (unpaired two-sample t-test). **h**, Schematic diagram summarizing NPC preparation for proliferation assay and representative scatter plot showing cells in each cycle phase (G1, S and G2/M). **i**, No significant differences in percentage of the BrdU-positive population between TD, typical WS and pWS88 NPCs. **j**, Schematic diagram summarizing NPC preparation for apoptosis analysis and representative analysed data for DNA fragmentation (left) and caspase assay (right). **k–m**, Changes in ratio of NPC number on day 4 over day 0 relative to TD (**k**), percentage of subG1 population (**l**) and percentage of population with high caspase activity (**m**) of pWS88 NPCs when treated with shFZD9 and shControl. **n**, Increase in cell number day 4/day 0 upon overexpression of FZD9 in WS iPSC-derived NPCs. Data are shown as mean $\pm$ s.e.m. for each individual; n, technical replicates. For **i** and **k–m**, data are shown as mean $\pm$ s.e.m.; n, number of clones, *$P < 0.05$, **$P < 0.01$, ***$P < 0.001$, one-way ANOVA and Tukey's post hoc test (**i**), Kruskal–Wallis test and Dunn's multiple comparison test (**k–m**).

Extended Data Figure 5 | Single-cell analysis of WS and TD iPSC-derived neurons. a, **b**, Outlier exclusion based on limit of detection = 24, analysed by Fluidigm Singular 3.0. Outliers were removed manually on the basis of the sample median log$_2$(expression) values. **c**, Heat map of number of genes with ANOVA $P < 0.05$ (82 genes in total). **d**, Unsupervised hierarchical clustering of 672 single-cell of WS and TD iPSC-derived neurons identified cell sub-populations not linked with the genotype.

Cells are shown in rows and genes in columns. Log$_2$(gene expression levels) were converted to a global Z-score (blue is the lowest value, red is highest). Genes were clustered using the Pearson correlation method and cells were clustered using the Euclidean method. **e**, PCA projections of the 96 genes, showing the contribution of each gene to the first two PCs. **f**, Violin plots of all 96 genes showing the comparison between TD, WS and pWS88 neurons from the single-cell analyses (log$_2$(expression) values).
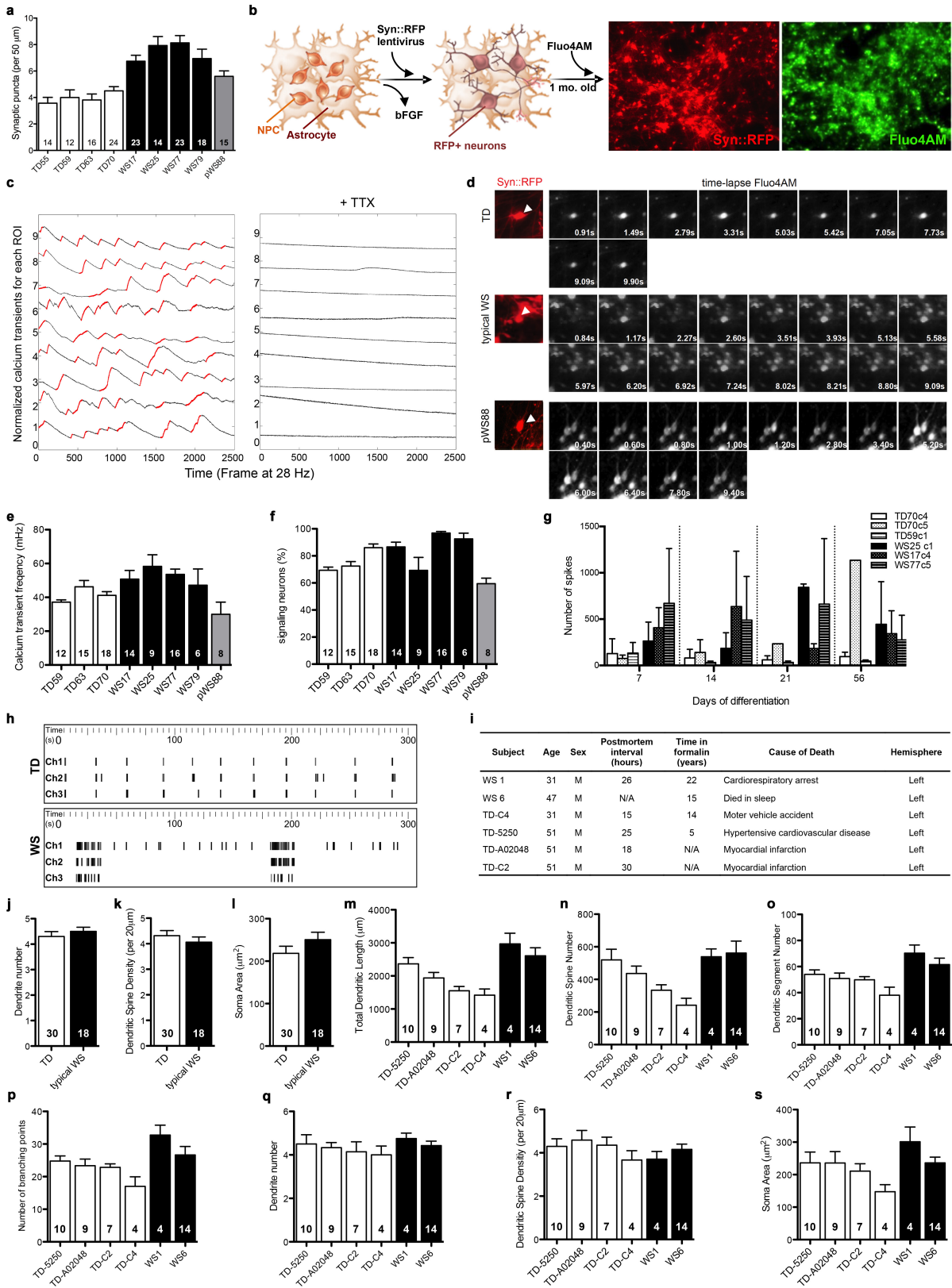
Extended Data Figure 6 | See next page for caption.

Extended Data Figure 6 | Morphometric analysis of WS-derived CTIP2-positive cortical neurons. a, Summary of preparation of neurons for evaluation by morphometric analysis. **b**, Representative images of EGFP- and CTIP2-positive neuron (arrowhead) and tracing. Scale bar, 200 μm. **c–f**, No significant differences in dendritic segment numbers (**c**), number of branching points (**d**), dendritic spine density (**e**) and soma area (**f**) between TD, typical WS and pWS88 were observed. **g–m**, Morphometric analysis shown as individual participant for total dendritic length (**g**), dendritic tree number (**h**), dendritic spine number (**i**), dendritic segment number (**j**), number of branching points (**k**), dendritic spine density (**l**) and soma area (**m**). **n**, Four-week-old neurons were dissociated and plated to trace total neurite length every hour, for a total of 6 h. Representative images of traced neurons plated after 0 and 6 h from TD, typical WS and atypical pWS88 iPSC-derived neurons. **o–r**, Morphometric analysis showing significant differences among TD, typical WS and pWS88 in the initial neurite growth velocity (6 h period). **r**, Morphometric analysis shown for individual participants for neurite growth velocity for 6 h interval. *n*, Number of traced neurons. **s–u**, No significant changes were observed in the total dendritic length (**s**), dendritic segment number (**t**) and dendritic spine number (**u**) of TD neurons plated in different densities (300–1,200 cells per square millimetre). **v**, Individual channels of puncta quantification of post- and presynaptic markers (Homer1/Vglut1). Scale bar, 2 μm. For **c–m** and **o–u**, data are shown as mean ± s.e.m.; *n*, number of traced neurons, *$P < 0.05$, **$P < 0.01$, Kruskal–Wallis test (**c–f**), one-way ANOVA and Tukey's post hoc test (**o–q**, **r–u**).

Extended Data Figure 7 | See next page for caption.

Extended Data Figure 7 | Alteration in calcium transient in WS iPSC-derived neurons and morphometric analysis of cortical layer V/VI pyramidal neurons in post-mortem tissue. a, Puncta quantification of post- and presynaptic markers. The synaptic proteins Vglut (presynaptic) and Homer1 (postsynaptic) were used as markers and only co-localized puncta on MAP2^{+} cells were quantified and graphed. Data are shown as the mean ± s.e.m.; *n*, number of neurons. **b**, Summary of preparation of neurons for calcium transient analysis. Representative images of live neuronal culture expressing RFP driven by synapsin promoter and the uptake of Fluo-4AM calcium dye. **c**, Blockade of calcium transient by TTX inhibition of synaptic activity. **d**, Representative images of calcium transient in single neurons (RFP-positive, arrowhead) from TD (top), typical WS (middle) and pWS88 (bottom). Number in the lower right of each figure represents each time point (seconds) when change in Fluo-4AM occurs. **e**, **f**, Calcium transient analysis shown as individual for frequency (**e**) and percentage of signalling neurons (**f**). Data are shown as mean ± s.e.m.; *n*, number of fields analysed. **g**, MEA analyses revealed an increase in spontaneous neuronal spikes. Data show individual clones. **h**, Raster plot of TD and WS iPSC-derived neurons analysed by multi-electrode array. **i**, Details of individuals used for the analysis. **j–l**, No significant differences in dendrite number (**j**), dendritic spine density (**k**) and soma area (**l**) between TD and typical WS were observed. Data are shown as mean ± s.e.m.; *n*, number of traced neurons, two-sided unpaired Student's *t* test. **m–s**, Morphometric analysis shown for each individual for total dendritic length (**m**), dendritic spine number (**n**), segment number (**o**), branching point number (**p**), dendrite number (**q**), dendritic spine density (**r**) and soma area (**s**). Data are shown as mean ± s.e.m.; *n*, number of traced neurons.

Extended Data Table 1 | List of top ten most significant differentially expressed genes in WS compared with TD for NPC and neurons

NPC: TD x WS

Gene name	Description	Fold-change	p-value
SCN4A	sodium channel, voltage gated, type IV alpha subunit	-11.92	9.72E-10
SLC7A14	solute carrier family 7, member 14	-15.85	1.85E-12
SLC38A5	solute carrier family 38, member 5	-8.51	5.67E-09
ADGRA2	adhesion G protein-coupled receptor A2	-30.50	3.26E-08
SLC1A6	solute carrier family 1 (high affinity aspartate/glutamate transporter), member 6	8.03	1.56E-08
CXCL12	chemokine (C-X-C motif) ligand 12	-7.51	3.33E-08
SLC30A3	solute carrier family 30 (zinc transporter), member 3	10.28	8.32E-09
SLC8A2	solute carrier family 8 (sodium/calcium exchanger), member 2	-16.84	5.36E-13
HTR1B	5-hydroxytryptamine (serotonin) receptor 1B, G protein-coupled	-10.96	8.20E-09
SLC24A2	solute carrier family 24 (sodium/potassium/calcium exchanger), member 2	-13.25	4.43E-10

NPC: TD x pWS88

Gene name	Description	Fold-change	p-value
GABRA3	gamma-aminobutyric acid (GABA) A receptor, alpha 3	14.71	6.30E-10
SYT13	synaptotagmin XIII	6.55	1.87E-08
PPP2R2C	protein phosphatase 2, regulatory subunit B, gamma	15.74	7.69E-09
CELF4	CUGBP, Elav-like family member 4	7.27	1.22E-07
TRIM67	tripartite motif containing 67	15.08	6.52E-10
ADRA2A	adrenoceptor alpha 2A	8.44	1.42E-07
JAKMIP1	janus kinase and microtubule interacting protein 1	19.56	7.21E-09
CA10	carbonic anhydrase X	74.54	8.50E-10
LHFPL4	lipoma HMGIC fusion partner-like 4	8.31	5.71E-08
ACSL6	acyl-CoA synthetase long-chain family member 6	7.07	7.63E-08

Neuron: TD x pWS88

Gene name	Description	Fold-change	p-value
CRYM	crystallin, um	7.68	3.21E-05
RASL12	RAS-like, family 12	13.41	6.04E-08
PDLIM1	PDZ and LIM domain 1	5.44	1.00E-05
ZSCAN10	zinc finger and SCAN domain containing 10	58.80	6.22E-06
ANO1	anoctamin 1, calcium activated chloride channel	9.61	1.78E-06
DUSP23	dual specificity phosphatase 23	5.09	0.000114507
SLC16A5	solute carrier family 16 (monocarboxylate transporter), member 5	33.27	8.90E-05
KRT19	keratin 19, type I	9.94	0.000130985
TMEM30B	transmembrane protein 30B	17.09	2.11E-07
KIF18B	kinesin family member 18B	4.50	0.000217123

Neuron: TD x WS

Gene name	Description	Fold-change	p-value
FAM19A5	family with sequence similarity 19 (chemokine (C-C motif)-like), member A5	1076.39	2.23E-10
TPM2	tropomyosin 2 (beta)	-5.88	2.99E-08
SCN4A	sodium channel, voltage gated, type IV alpha subunit	-45.81	1.63E-07
IGSF21	immunoglobin superfamily, member 21	8.20	2.33E-07
TNNT2	troponin T type 2 (cardiac)	-29.87	3.58E-07
PXMP4	peroxisomal membrane protein 4, 24kDa	-7.39	3.83E-05
ZSCAN10	zinc finger and SCAN domain containing 10	35.64	9.74E-05
MYOZ1	filamin-, Actinin- And Telethonin-Binding Protein	-6.64	0.000119159
LAD1	ladinin 1	-24.81	0.000213205
PHOSPHO1	phosphatase, Orphan 1	33.95	0.000266061

Extended Data Table 2 | Most significant ($P < 0.05$) enriched GO terms in NPC of WS compared with TD samples

Down-regulated genes in WS compared to TD in NPC cells

GO TERM	GO Description	-Log (p-value)	P-value	Genes
GO:0005578	proteinaceous extracellular matrix	18.3452855	4.52E-19	WNT16,MMP25,DCN,LAMC3,COL16A1,WNT11,ADAMTS2,LAMB1,PAPLN,MMP9,WISP1,ECM2,COL1A1,CPZ,EFEMP1,LTBP2,COL10A1,COL21A1,OMD,ADAMTS8,WNT10A,EMILIN1,ADAMTS14,KERA,FBLN5,ADAMTS17,COL6A1,COL6A2,ADAMTS10,HMCN1,ADAMTS16,HAPLN1,ADAMTS4,COL6A3,COL1A2,MFAP4,SOST,NPNT,COL6A5,HPSE2,VWC2,PRELP,SPOCK3,LAMA2,ADAMTSL2,COL28A1
GO:0048856	anatomical structure development	16.80415844	1.57E-17	WNT16,MYLIP,TFAP2B,BAZ1B,CD4,DCN,SEMA3B,ADGRA2,RUNX3,IBSP,TG,ALX4,CAMK2B,TLE2,MAOB,RORA,EPHA8,TP63,PLXNA2,RARB,MEF2C,WNT11,TFAP2C,LAMB1,DSP,NEFH,MMP9,HCK,SGCG,FLT1,CRISPLD2,CPQ,MET,COBL,ENG,PITX3,COL1A1,CPT1A,CYP27B1,VDR,EYA4,TFEB,PCDHB2,PCDHB5,PCDHB6,PDGFRB,FN1,TFAP2E,LPPR4,RCAN3,TNNT2,BCL11A,PCDHB14,PCDHB12,INHBA,COL10A1,BMP2,TCF15,SIX1,HSPA2,PTPRB,CDH15,SERPINF1,LYVE1,PDGFRA,TBX3,HEY2,AGT,WNT10A,RAPGEF5,MYO7A,MSTN,ARHGAP24,CDH11,COL6A1,COL6A2,ITGA10,ELF3,SERPINI1,HEYL,PITX2,NPY1R,NPY5R,ITGA2,DACT2,COL1A2,SYK,DACT1,ANPEP,BATF2,NPNT,EFNA1,GPR183,BNC1,ALCAM,SIX2,SGCD,HAS2,PTGER4,NINJ2,SCG2,RARG,SSH3,ABLIM3,CSPG4,CMKLR1,LY6H,PCDHB9,TH,MAB21L1,GREM2,ADGRB1,FES,CSF1R,NTM,CAMK1D,GAS6,OPCML,SCN5A,TBX1,ALDH1A3,SLITRK6,SGCZ,TNFAIP2,NTF3,RTN4RL1,PDE2A,DNER,VWC2,PRELP,TDRD7,AKR1C3,RYR1,MME,LAMA2,PCDHB11,PAPSS2,MAFB,POU5F1,PCDHA7,PCDHA5,DPF3,ITGA1,GSTA1,PCDHA11,PCDHA10
GO:0007155	cell adhesion	16.70678997	1.96E-17	CD4,CLDN11,IBSP,TNC,LAMC3,RORA,EPHA8,COL16A1,LAMB1,FERMT1,HCK,SRPX,WISP1,ECM2,ENG,CXCL12,PRPH2,PCDHB2,PCDHB5,PCDHB6,FN1,PCDH17,PCDHB14,PCDHB12,ADGRE5,TNFAIP6,OMD,ADGRE2,ISLR,CDH15,MYBPH,LYVE1,PDGFRA,EMILIN1,PCDH10,FBLN5,CDH11,COL6A1,COL6A2,ITGA10,HAPLN1,CNTNAP5,ITGB2,AZGP1,SNED1,COL6A3,IGFBP7,ITGA2,EDIL3,SYK,MFAP4,NPNT,EFNA1,PCDH7,ALCAM,LRRN2,PTGER4,NINJ2,COL6A5,PCDHB9,ADGRB1,NTM,GAS6,OPCML,PKP3,THBS2,LAMA2,PCDHB11,ITGBL1,PCDHA7,PCDHA5,ITGA1,COL28A1,PCDHA13,PCDHGC3,ACTN3,PCDHA11,PCDHA10,PCDHGA7
GO:0030198	extracellular matrix organization	13.94978657	1.12E-14	DCN,IBSP,TNC,LAMC3,COL16A1,ADAMTS2,LAMB1,MMP9,ENG,COL1A1,EFEMP1,FN1,COL10A1,COL21A1,BMP2,EMILIN1,ADAMTS14,FBLN5,COL6A1,COL6A2,ITGA10,CTSK,HAPLN1,MMP14,ADAMTS4,ITGB2,CTSS,COL6A3,ITGA2,KLKB1,COL1A2,MFAP4,LTBP3,NPNT,HAS2,COL6A5,GAS6,LAMA2,ITGA1,COL28A1
GO:0005576	extracellular region	9.533946889	2.92E-10	WNT16,SCIN,MMP25,SYT7,DCN,SEMA3B,CLDN11,GPRC5A,ACPP,EHD2,IBSP,TNC,FAM65C,TG,LAMC3,ENTPD2,LY75,TLE2,BCL3,MAOB,FRMPD1,COL16A1,WNT11,ADAMTS2,LAMB1,DSP,SUSD2,APOL4,PAPLN,MMP9,BPI,MCF2,PLP2,ACP5,FLT1,WFDC1,CRISPLD2,CRYM,PDGFRL,CPQ,WISP1,NDRG1,MET,STX1A,PCOLCE,ECM2,ENG,PTGDS,CXCL12,PNPO,COL1A1,CPZ,OAS3,PDGFRB,POMC,EFEMP1,FN1,IL1R1,QPCT,ANGPTL1,VAMP8,LTBP2,ENOX1,CAT,CPXM2,XPNPEP2,INHBA,ADGRE5,COL10A1,EDN3,COL21A1,CPNE5,BMP2,PCSK2,CFP,HSPA2,OMD,TUBA4A,FGL2,ISLR,CDH15,DPP6,SERPINF1,GSTT2B,LYVE1,IAH1,ADAMTS8,DYSF,AGT,WNT10A,EMILIN1,ADAMTS14,MSTN,RBP5,KERA,SLC46A3,FBLN5,ADAMTS17,CDH11,COL6A1,COL6A2,NTN5,ADAMTS10,FCN3,HMCN1,CTSK,LEFTY2,TMEFF2,ADAMTS16,HAPLN1,GABRB2,PLA2G7,IGSF1,LCN9,SLC5A12,CCDC3,IGSF10,PLA2R1,TMPRSS11D,MMP21,GNA14,WIF1,NBL1,FGF17,ADAMTS4,STC1,C1R,ITGB2,PTH1R,AZGP1,FGFR4,PLXDC1,CXCL16,ITIH3,BRINP3,SNED1,HAAO,CTSS,S100A11,COL6A3,IGFBP7,SERPINI1,ALB,CDCP1,PRSS12,EDIL3,KLKB1,COL1A2,CHMP4C,AKR1E2,VWA2,MFAP4,ACSM1,ANPEP,GPT,SOST,LTBP3,NPNT,FSTL5,EFNA1,ALCAM,CYTL1,SOSTDC1,SCG2,COL6A5,HPSE2,CSPG4,ADGRG2,C1QTNF1,VPS37D,CLEC14A,EPS8L2,GREM2,PENK,C1S,GRID1,GAS6,OPCML,OLFML1,ALDH1A3,FAM19A3,MUC6,TNFAIP2,FAM212A,NTF3,RTN4RL1,THBS2,THSD4,VWC2,PRELP,PLAC9,SPOCK3,HLA-DRB1,AKR1C3,RYR1,MME,LAMA2,ADAMTSL2,SULT1C2,HLA-DRB5,ITGBL1,RASSF9,TGM2,ITGA1,COL28A1,APOL6,PCDHGC3,GSTA1,C4A,ACTN3,PCDHA10
GO:0005615	extracellular space	8.287607079	5.16E-09	WNT16,DCN,ACPP,IBSP,TNC,TG,TLE2,WNT11,LAMB1,APOL4,MMP9,FLT1,WFDC1,CPQ,WISP1,PCOLCE,ENG,PTGDS,COL1A1,OAS3,POMC,EFEMP1,FN1,ANGPTL1,LTBP2,ENOX1,CPXM2,INHBA,ADGRE5,EDN3,BMP2,PCSK2,CFP,HSPA2,FGL2,SERPINF1,AGT,WNT10A,MSTN,FBLN5,COL6A2,FCN3,CTSK,LEFTY2,PLA2G7,NBL1,FGF17,ADAMTS4,C1R,AZGP1,PLXDC1,CXCL16,CTSS,S100A11,COL6A3,IGFBP7,SERPINI1,ALB,KLKB1,COL1A2,VWA2,ACSM1,ANPEP,SOST,CYTL1,SOSTDC1,SCG2,C1QTNF1,C1S,GAS6,TNFAIP2,VWC2,SPOCK3,C4A
GO:0005886	plasma membrane	8.166494631	6.82E-09	CALCR,ABCC8,TBXA2R,SCN4A,CACNA2D2,MYLIP,MMP25,CD4,HFE,CLDN11,GPRC5A,ACPP,SLC38A5,ATP1A2,ADGRA2,EHD2,PTGER3,CYBA,ENTPD2,LY75,MCOLN3,CAMK2B,FRMPD1,CNGB1,EPHA8,MGLL,PLXNA2,PAG1,ATP8B1,IL12RB2,KCNK2,GABRP,DSP,KCNK6,SUSD2,SLC10A1,SLC8A3,FERMT1,HCK,BPI,PLP2,NALCN,SGCG,FLT1,NDRG1,MET,VIPR2,COBL,STX1A,ENG,RNF43,TCIRG1,TNS2,KCNA1,OAS3,ADGRD1,PCDHB2,PCDHB5,PCDHB6,SLC27A6,PDGFRB,IL1R1,LPPR4,SLC8A2,SGK1,VAMP8,PCDH17,GPR68,GRIA2,PCDHB14,PCDHB12,ENOX1,XPNPEP2,ADGRE5,PMEPA1,HSPA2,PTPRB,ADGRE2,ADCY4,CDH15,ATP1A4,LYVE1,TRPM1,PDGFRA,HTR1B,DYSF,SLC19A3,PCDH10,FBLN5,DISP2,CDH11,BEST4,ITGA10,RGS16,UNC80,SLC22A14,EPHA5,GABRB2,SLC22A3,HTR2C,SLC26A7,SLC5A12,PLCH2,LYPD6B,CACNA2D4,CACNA1C,ANO4,EDNRA,GABRA2,PLA2R1,TMPRSS11D,MCOLN2,FGD5,SLC24A2,GNA14,MMP14,CACNA1D,LYPD5,ABCG1,ITGB2,PTH1R,AZGP1,FGFR4,LY6E,PLXDC1,ALOX15,CXCL16,DHRS3,FZD5,CDCP1,MST1R,PRSS12,NPY1R,NPY5R,ITGA2,KLKB1,ACSL6,GRIK2,HCN1,SYK,ANPEP,PARM1,AFAP1L2,GSG1L,EFNA1,PTAFR,NPR1,GPR183,PCDH7,TM4SF1,SLC16A5,SIX2,SGCD,PRKCDBP,HAS2,KCND3,PTGER4,NINJ2,SYNPO,GPR22,HPSE2,EVC2,BNC2,CSPG4,ADGRG2,C1QTNF1,CMKLR1,SLCO3A1,LY6H,EPS8L2,PCDHB9,TH,GPR139,ADGRB1,FES,CSF1R,NTM,GRID1,RGS7,OPCML,SCN5A,PKP3,SLITRK6,TMEM173,ANKS1B,SGCZ,IFNLR1,PRKG1,EVI2B,RTN4RL1,PDE2A,TPCN1,QRFPR,NPSR1,GJA4,DNER,OR7D2,CLEC2A,NKAIN2,HLA-DRB1,RYR1,MME,CHRNG,PCDHB11,HLA-DRB5,PPAPDC1A,PCDHA7,PCDHA5,ITGA1,PCDHA13,PCDHGC3,C4A,FMN1,PCDHA11,PCDHA10,PCDHGA7
GO:0055085	transmembrane transport	7.872963268	1.34E-08	ABCC8,SCN4A,CACNA2D2,SLC7A14,SLC38A5,ATP1A2,MCOLN3,ATP2C2,CNGB1,ATP2A3,RARB,SLC25A43,ATP8B1,KCNK2,FXYD5,SLC17A6,GABRP,KCNK6,SLC10A1,SLC8A3,PLP2,NALCN,CPT1A,TCIRG1,KCNA1,SLC27A6,PEX5L,STEAP3,SLC8A2,SGK1,GRIA2,ADCY4,ATP1A4,TRPM1,ADAMTS8,SLC19A3,SLC46A3,BEST4,CASQ1,UNC80,SLC22A14,SLC25A48,GABRB2,SLC22A3,SLC26A7,SLC5A12,CACNA2D4,CACNA1C,ANO4,GABRA2,MCOLN2,SLC24A2,CACNA1D,ABCG1,AZGP1,COX7A1,ALB,GRIK2,HCN1,SLC16A5,KCND3,RARG,SLCO3A1,SLC17A8,SLC9A9,GRID1,SLC25A18,GAS6,SCN5A,PDE2A,TPCN1,RYR1,CHRNG

Up-regulated genes in WS compared to TD in NPC cells

GO TERM	GO Description	-Log (p-value)	P-value	Genes
GO:0007155	cell adhesion	2.964750421	0.00108455	ITGB5,TNR,TEK,PARVG,CDHR1,MPZL2,GRID2,ACAN,PIK3CD,EGFL7,CLDN6,GCNT1,CLDN4,PTPRT,DPP4
GO:0005886	plasma membrane	2.391582019	0.00405899	GABRA3,ERBB3,ITGB5,TNFRSF10A,SLC1A6,SLC6A12,GLP1R,SLC30A3,ABCG2,TEK,CSMD2,SDC4,BTN1A1,F12,PDE6B,MAP7,PARVG,RHCG,PPAP2C,ZNF185,PLIN2,CDHR1,KIRREL3,DLG2,GPR158,GRID2,ADCY8,XKR8,F11R,CLIC6,WNT4,OXGR1,OSCAR,PIK3CD,MRGPRF,GRM8,KCNB2,EPHA10,ADRA2C,CLDN6,CLDN4,PTPRT,DPP4,OCLN,CD247,HLA-DOA,SHISA9,HLA-DMB
GO:0006629	lipid metabolic process	2.063032094	0.00864904	ST3GAL6,ST8SIA5,SDC4,APOC1,CYP2J2,CYP11A1,PPAP2C,PLIN2,WNT4,HACD1,PIK3CD,ACOT12,FADS6,UGT8,SPTSSB
GO:0007009	plasma membrane organization	1.872296029	0.0134185	MAP7,XKR8,F11R,WNT4
GO:0006790	sulfur compound metabolic process	1.823703224	0.0150071	MGST1,ST3GAL6,SDC4,ACOT12,OPLAH,CHST6
GO:0007267	cell-cell signaling	1.725551179	0.0188126	GABRA3,PTPRN,SLC1A6,SLC6A12,TEK,DLG2,GRID2,ADCY8,KCNB2,MAFA,ADRA2C
GO:0048856	anatomical structure development	1.689882589	0.0204229	ERBB3,MYLK,ITGB5,HTATIP2,TNR,HPCAL4,PADI2,TEK,LIN28A,CHI3L1,TMOD1,RHCG,RP11-35N6.1,KIRREL3,MPZL2,DLG2,GRID2,ACAN,F11R,WNT4,HACD1,KRT19,PIK3CD,EGFL7,UGT8,ALX1,EPHA10,ADRA2C,CLDN4
GO:0005576	extracellular region	1.604486647	0.0248607	ST3GAL6,ERBB3,MYLK,ITGB5,ZDHHC15,CPVL,ENPP5,TNR,PADI2,TEK,NPPB,SDC4,BTN1A1,SPINK2,PRRG3,APOC1,F12,CHI3L1,CYP2J2,RHCG,CBLC,PLIN2,KIRREL3,ACAN,ITLN2,F11R,VWA5B1,CLIC6,WNT4,MUC3A,OSCAR,KRT19,EGFL7,MRGPRF,CREG2,EPHA10,BEX5,ADAMTSL5,PABPC1L2A,DPP4,GPX3,FAM19A5
GO:0007010	cytoskeleton organization	1.404009141	0.0394449	MYLK,ITGB5,CORO2A,MAP7,TMOD1,PARVG,F11R,CDC42BPG,KRT19
GO:0016757	transferase activity, transferring glycosyl groups	1.395223326	0.040251	ST3GAL6,ST8SIA5,GALNT14,UGT8,GCNT1

Extended Data Table 3 | Most significant (*P* < 0.05) enriched GO terms in neurons of WS compared with TD samples

Down-regulated genes in WS compared to TD in neurons

GO TERM	GO Description	-Log(p-value)	P-value	Genes
GO:0043167	ion binding	2.995842055	0.00100962	BAZ1B,FMO1,VRK2,DSG2,RFC2,ME1,ATP2A3,ADAMTS2,MYL9,TNNC2,ENO3,FOLR1,ACSS3,TRIM38,PCDHB5,TNNC1,ABCG2,CAT, ADGRE5,MYH2,ADGRE2,ZNF835,ATP8B3,MTL5,GSTM1,ACTA1,SH3RF2,ACTC1,ALOX15,CAPN13,ZNF283,ZNF558,ACOX2,GSTM4, SLFN12,RHOD,RNF212,ZNF626,SERPINA5,S100A13,S100A4,ZNF502,ZFP28,ZNF560,ZNF667,PEG3,ZNF726,ZNF737,ZNF578
GO:0008092	cytoskeletal protein binding	2.841323964	0.00144104	USH1C,MYBPC2,TNNC2,STX1A,TNNC1,TNNT2,MYH2,ACTA1,ACTC1,MYOZ1,TPM2
GO:0003013	circulatory system process	2.42626763	0.00374742	ELN,TNNC1,AGT,ACTC1,CD34
GO:0006950	response to stress	2.270514469	0.00536396	TBXA2R,BAZ1B,VRK2,RFC2,ATP2A3,IL4R,LAT2,MYL9,TRIM38,CAT,ADGRE5,MYH2,ADGRE2,MTL5,GSTM1,PARP9,ALOX15,ACOT11, BATF2,CD34,BHLHA15,SIGIRR,IFITM2,SERPINA5,HLA-DRB1,HLA-DRB5,POU5F1
GO:0005198	structural molecule activity	2.015682009	0.00964535	MYOM2,ELN,MYBPC2,MYL9,MYH2,TINAGL1,ACTA1,LAD1,TPM2
GO:0005829	cytosol	1.675077895	0.0211311	USH1C,ME1,MYBPC2,MYL9,TNNC2,STX1A,EIF4H,ENO3,TRIM38,TNNC1,TNNT2,MYH2,GSTM1,PARP9,ACTA1,ACTC1,ALOX15, GSTM4,RHOD,ALDH1A3,S100A13,TPM2,POU5F1
GO:0005777	peroxisome	1.574933909	0.0266113	PXMP4,CAT,ACOX2
GO:0003674	Molecular function	1.54856974	0.0282768	USH1C,TBXA2R,SCN4A,BAZ1B,FMO1,ACPP,VRK2,MYOM2,DSG2,PREX2,ELN,RFC2,ME1,ATP2A3,IL4R,LAT2,MYBPC2,ADAMTS2, PROKR2,MYL9,PXMP4,TNNC2,STX1A,TBL2,EIF4H,ENO3,FOLR1,ACSS3,TRIM38,SLC22A2,PCDHB5,SLC27A6,TNNC1,TNNT2, ABCG2,CAT,ADGRE5,MYH2,ADGRE2,ZNF835,ATP8B3,NSUN5,MTL5,DMGDH,GSTM1,AGT,THUMPD2,PARP9,TINAGL1,ACTA1, RASSF3,SH3RF2,LAD1,ACTC1,ALOX15,ACOT11,UBXN10,CAPN13,RBM47,TC2N,ZNF283,ZNF558,BATF2,ACOX2,GSTM4,CYTL1, PRKCDBP,SLFN12,RHOD,CD34,CHRNA9,GCNT4,MYOZ1,RNF212,BHLHA15,MAATS1,ALDH1A3,RNLS,RBM43,SIGIRR,CCK, ZNF626,LRRIQ4,SERPINA5,S100A13,HLA-DRB1,S100A4,ZNF502,ZFP28,SLC2A10,ZNF560,ZNF667,PEG3,TPM2,HLA-DRB5,LAYN, POU5F1,ZNF726,ANKRD65,ZNF737,ZNF578,SLC22A31,TCF24
GO:0016765	transferase activity, transferring alkyl or aryl (other than methyl) groups	1.475366347	0.0334683	GSTM1,GSTM4
GO:0016887	ATPase activity	1.459248951	0.0347337	RFC2,ATP2A3,TNNT2,ABCG2,ATP8B3,ACTC1
GO:0016874	ligase activity	1.406285389	0.0392387	RFC2,ACSS3,TRIM38,SLC27A6,SH3RF2,RNF212
GO:0015979	photosynthesis	1.387345392	0.0409878	RFC2
GO:0005615	extracellular space	1.320715681	0.0477842	ACPP,ENO3,ADGRE5,AGT,TINAGL1,ACTA1,ACTC1,CYTL1,SERPINA5,S100A13,S100A4

Up-regulated genes in WS compared to TD in neurons

GO TERM	GO Description	-Log(p-value)	P-value	Genes
GO:0001071	nucleic acid binding transcription factor activity	2.409059017	0.00389889	PITX1,TFAP2C,HAND1,NR5A2,IRF6,ZSCAN10,KLF4,ALX1,DMBX1,FOXB2
GO:0008233	peptidase activity	1.531733923	0.0293945	HPN,PRSS16,RHBDF2,ADAMTS16,USP41,TMPRSS2
GO:0009790	embryo development	1.354676981	0.0441899	HPN,HAND1,NR5A2,KLF4
GO:0006091	generation of precursor metabolites and energy	1.330439536	0.0467262	ALDOC,MT-ND2,MT-ND4,MT-ND1
GO:0048856	anatomical structure development	1.312454095	0.0487019	PITX1,TFAP2C,HPN,ALDOC,HAND1,NR5A2,IRF6,ZSCAN10,KLF4,PRDM14,BMP6,ISL2,PROK2,PHOSPHO1,ALX1,DMBX1